

Method for Determining Adiabatic Film Effectiveness in Presence of Thermal Boundary Layer

James Parker

Department of Engineering Science,
Osney Thermofluids Institute,
University of Oxford,
Parks Road,
Oxford OX1 3PJ, UK
e-mail: james.parker@univ.ox.ac.uk

Thomas Povey¹

Department of Engineering Science,
Osney Thermofluids Institute,
University of Oxford,
Parks Road,
Oxford OX1 3PJ, UK
e-mail: thomas.povey@eng.ox.ac.uk

In this paper, we present a new method for determining adiabatic film effectiveness in film cooling experiments with nonuniform inlet temperature distributions, in particular the situation of an inlet thermal boundary layer. This might arise in a quasi-steady experiment due to loss of heat from the mainstream flow to the inlet contraction walls, for example. In this situation, the thermal boundary layer would be time-varying. Adiabatic film effectiveness is generally normalized by the difference between mainstream and coolant gas temperatures. Most importantly, these temperatures are generally assumed to be spatially—and, possibly temporally—uniform at the system inlet. In experiments with nonuniform inlet temperature, the relevant hot gas temperature for a particular point of interest on a surface is not easily determined, being a complex function of both the inlet temperature profile and the flow field between the inlet and the point of interest. In this situation, adiabatic film effectiveness cannot be uniquely defined using conventional processing techniques. We solve this problem by introducing the concept of equivalent mainstream effectiveness, a nondimensional temperature for the mainstream that can be used to represent the thermal boundary layer profile at the inlet plane, or the effective temperature of the mainstream gas—which we refer to as the equivalent mainstream temperature—entrained into the mixing layer affecting the wall temperature at a particular point of interest. By using data from two or more time instants during an experiment, we simultaneously solve for equivalent mainstream effectiveness and true adiabatic film effectiveness, that is, the adiabatic film effectiveness that we would measure in an experiment with both steady and uniform inlet temperature. This is an important transformation because the true adiabatic effectiveness has a clear physical interpretation and is a more transportable quantity between systems (comparisons between different experiments, between experiment and computational fluid dynamics (CFD), etc.). The proposed method is experimentally demonstrated using full-surface infrared (IR) thermography measurements of a cooled rotor blade platform, operated in a transonic linear cascade facility at matched engine conditions. Film effectiveness measurements processed in the conventional way suffer from inlet thermal boundary layer effects, rendering them both time-varying (as heat is released to the walls of the tunnel) and, in certain regions, nonphysical in magnitude. The proposed technique renders the same data insensitive to time, and everywhere within physically reasonable limits. By demonstrating independence to the particular (time-varying) inlet temperature profile, we demonstrate the advantages of the proposed technique.

[DOI: 10.1115/1.4053021]

Keywords: boundary layer development, cavity and leakage flows, heat transfer and film cooling, measurement techniques, turbine blade and measurement advancements

Introduction

Film cooling performance is often characterized using the adiabatic film effectiveness, η , a nondimensional temperature typically defined by

$$\eta = \frac{T_{01} - T_{w,ad}}{T_{01} - T_{02}} \quad (1)$$

where $T_{w,ad}$ is the adiabatic surface temperature at a point of interest, T_{01} is the (typically hot) mainstream gas temperature, and T_{02} is the (typically cold) coolant gas supply temperature.

In an adiabatic system, the wall temperature can be thought of as being due to mixing of particular mass fractions of hot and cold gas at the surface. In this sense, the adiabatic film effectiveness can be regarded as being directly related to the local mass fractions. More

specifically, rearranging (1), we write

$$T_{w,ad} = \eta T_{02} + (1 - \eta) T_{01} \quad (2)$$

where η can now be thought of as the mass fraction of cold gas and $(1 - \eta)$ the mass fraction of hot gas. Strictly speaking, this formulation is only valid in the case of the mainstream and coolant stream having the same specific heat capacity. This is approximately true in the vast majority of experimental situations, and we adopt this simplification in the remainder of this paper. An extension of the arguments to situations where the heat capacities are not the same is possible with some additional complexity in the formulation.

It is common practice to use laboratory experiments at reduced temperature to optimize film cooling systems for engines. One part of this optimization may be the adiabatic film effectiveness distribution. Provided the temperature *ratio* (TR) is matched, to first order the laboratory measurements will be the same as the expected engine condition and require no further scaling. In cases where the temperature ratio is not matched, and where air is used for both coolant flow and mainstream flow, the scaling can be quite complex (see, for example, Ref. [1]). The need to scale arises

¹Corresponding author.

Contributed by the Heat Transfer Division of ASME for publication in the JOURNAL OF TURBOMACHINERY. Manuscript received December 1, 2020; final manuscript received August 11, 2021; published online January 13, 2022. Assoc. Editor: Jeffrey Bons.

primarily from a mismatch in the specific heat capacity flux ratio. This problem can be mitigated by using so-called *foreign gas* for one stream, typically the coolant stream, to bring the specific heat capacity flux ratio closer to the engine condition. Even if this approach is taken, second-order scaling issues would still need to be addressed [1].

However the experiments are run, and whatever the complexity of the scaling process required, all scaling processes fundamentally rely on the assumption of flow field—including mixing rate—similarity between the two environments (laboratory and engine). The primary driver for this in the case of adiabatic film cooling experiments is the momentum flux ratio between coolant and mainstream. More complex, second-order effects that lead to dissimilarity of the flow field are discussed in Ref. [1]. It is largely true to say that the second-order effects cannot be corrected for analytically, because they change the *structure* of the flow in a way that tends to be geometry specific. Thus, it is impossible to determine an analytical correction, or experimental correlation for the same.

In a well-designed experiment (that in which sufficient flow field similarity is achieved), to meaningfully use laboratory-measured adiabatic film effectiveness distributions to infer the equivalent engine property relies on η representing the mass fraction of cold gas. This is equally true regardless of whether significant scaling (mismatched temperature ratio and no foreign gas) or second-order scaling (matched temperature ratio or well-designed experiment using foreign gas) is required. If this assumption becomes unreasonable, the basis for equivalence in the two situations breaks down.

A problem arises when calculating values of adiabatic film effectiveness from Eq. (1) if the inlet temperature profile is nonuniform. An example of this is an inlet temperature profile caused by an inlet thermal boundary layer. In our example, we will refer to a wall which is cold relative to the hot mainstream gas. In this situation, the gas temperatures within the thermal boundary layer will be lower than that measured at mid-span. Streamlines at a range of temperatures within the boundary layer are convected into the downstream flow and entrained within the partially mixed-out coolant film that develops on the surface. The average temperature of the flow represented by these streamlines is unknown. It depends on the inlet gas temperature in the core-flow (that which is unaffected by the thermal boundary layer) and the wall temperature. In general, it is also a function of time. The adiabatic film effectiveness no longer represents the mass fraction of cold gas, and the meaning of the measured film effectiveness becomes ambiguous.

Achieving completely uniform (both spatially and temporally) inlet temperature profiles in experimental facilities is difficult and may reasonably—by inspection of the apparatus—be assumed to affect a significant proportion of heat transfer experiments to some degree. In particular, short duration, blowdown facilities, not dissimilar from the one used to collect data for this paper [2], are likely to have a time-dependent inlet thermal boundary layer, because the upstream surfaces do not reach steady-state conditions during the short test period (see also, for example, Refs. [3–5]).

The problem of arbitrariness in selecting a hot gas temperature in adiabatic film effectiveness measurements is seldom explicitly discussed in literature. The most common approaches are either using a single temperature measurement from the mainstream flow (normally the core-flow temperature), or taking an average of the inlet temperature profile by using a thermocouple rake. For the case of a cold thermal boundary layer, using the mainstream core-flow temperature would result in *inferred* effectiveness values greater than the value that would be obtained with an uniform inlet field; using the mean value could result in inferred effectiveness values either higher or lower than the values that would be obtained with an uniform inlet field. Thus, neither approach solves the central problem, and the resulting adiabatic film effectiveness values have ambiguous meaning and cannot easily be transported between environments (for comparison) or used to represent expected engine conditions (with or without scaling).

In this paper, we proposed a practical experimental processing technique which restores the direct link between adiabatic film

effectiveness and mass fraction in the experimental situation complicated by an inlet thermal boundary layer. We do this using the entire temporal response of the surface to simultaneously solve for local adiabatic film effectiveness, η , and a new local quantity which we refer to as *equivalent mainstream effectiveness*, η^* . The equivalent mainstream effectiveness can be thought of as a nondimensional expression for the mainstream flow temperature *associated with a particular point of interest*. This conceptual temperature could arise as the result of mixing of flow from regions of different temperature (streamlines emanating from different heights within the thermal boundary layer mixing before being entrained into the partially mixed coolant film), or convection of flow at a single temperature into the film cooling layer.

We demonstrate that adiabatic film effectiveness distributions from a single experiment in which a time-dependent thermal boundary layer is present can be reduced to equivalent distributions independent of the thermal boundary layer, and that these new distributions are therefore transportable to different environments (e.g., to predict engine performance). Complications arising from compressible effects are also briefly considered.

Related Literature

There are a number of well-established experimental techniques for the determination of adiabatic film effectiveness distributions from steady-state surface temperature measurements alone. These typically use IR thermography or thermochromic liquid crystal (TLC) methods. More advanced techniques, typically using one or more *transient* experiments, have been used to simultaneously determine both adiabatic film effectiveness and heat transfer coefficient distributions. In almost all these methods, it is assumed that the mainstream temperature is spatially uniform and that test surfaces can be modeled as semi-infinite surfaces (for transient heat conduction corrections). In more recent work, methods have also been proposed to determine the film effectiveness in the presence of a temporally constant but *spatially nonuniform* inlet temperature field (e.g., that arising from a combustor simulator). We review all these techniques below. It is notable that—in all the techniques we review—it is a requirement to assume that any inlet temperature nonuniformity is nonvarying with time. That is, it would not include the case in which there is a time-varying inlet thermal boundary layer. It is the case that almost all facilities suffer from a time-varying inlet thermal boundary layer—to some degree—and the purpose of this paper is to present a new method to account for this. In “Solution of the Equations” section, we show that it is possible to do this using a single transient run. The new method is applicable to many well-established experimental techniques and can be thought of as an additional processing step rather than a fundamentally new method.

Vedula and Metzger [6] proposed a two-test approach using the color transition of a TLC coating. In the first test, both mainstream and coolant flows were supplied at the same temperature, with the surface of interest conditioned to start at a uniform temperature different from the temperature of the flows. This surface was modeled as a semi-infinite surface with one-dimensional (1D) heat conduction. The local transition time of the liquid crystal was then used to determine the heat transfer coefficient at each surface location. In the second test, the coolant was heated with respect to the mainstream, and the surface heat transfer coefficient distribution used to calculate the driving surface temperature distribution, and the associated distribution of η . In this method, it is necessary to assume that the mainstream temperature is spatially uniform (no thermal boundary layer) so the relevant hot gas reference temperature is accurately known for all surface locations.

A related method was proposed by Ekkad et al. [7]. In a single transient experiment (IR thermography) with heated mainstream, surface images from two timestamps during the transient surface temperature rise were used to set up two simultaneous equations. These were solved at every location on the surface to yield

distributions of η and h . Reducing the method to a single experiment was reported to be advantageous in terms of both overall experimental time and uncertainty. The same assumptions about the mainstream temperature must be made as in the Vedula and Metzger [6] method.

More recently, Holgate et al. [8] proposed a technique in which η and h were determined in a single experiment. The proposed method does not require the surface material to be considered semi-infinite nor to have a uniform (in depth) initial temperature distribution. Experiments were characterized by an initial transient phase with increasing surface temperature followed by a period of approximately steady-state surface temperature. The test surface was made of a low thermal conductivity material with external film cooling, and unknown external h , and rear side cooling, at an assumed uniform internal h . They calculated η from time-averaged temperatures from the steady-state period of the run. The aerodynamic conditions and η were assumed constant throughout the experiment, including the transient phase. A finite-element model and the calculated distribution of η were then used in an iterative procedure to find a converged solution for the external distribution of h (each pixel from an IR camera image).

A number of techniques have been proposed to deal with the problem of spatially varying inlet temperature. To decouple the effects of film cooling on a HP NGV from additional cooling effects due to dilution gases in the inlet profile of a combustor simulator, Holgate et al. [9] proposed using a series of experiments, both with and without film cooling. The adiabatic film effectiveness when both dilution port flow and film cooling is present was assumed to consist of an apparent effectiveness from the dilution port flow, and an *additive film effectiveness* due to the film coolant itself. An experiment with dilution port flow and no film cooling was used to estimate the effectiveness due to dilution only and then remove this profile from the film effectiveness in the film and dilution experiment to yield an estimate of the additive film effectiveness.

Other techniques have been used to attempt to account for spatial variation in hot gas reference temperature in compressible flow environments. In the compressible situation, there is a superposed thermal gradient within the boundary layer due to a rise in static temperature as fluid decelerates in the near-wall region. This is often characterized by the local *recovery factor*, r [10], from which a *recovery temperature* $T_{01,R}$ can be defined, which depends on the local total temperature at the outer edge of the viscous boundary layer, and the local Mach number and Prandtl number. Since $T_{01,R}$ is a function of local Mach number, it can vary across a surface and therefore needs to be known at each location in order to determine η . Xue et al. [11] proposed a two-test technique, which allowed for the three unknown parameters η , h , and $T_{01,R}$ to be simultaneously determined. In the method, two tests are run using a hot mainstream temperature and two different coolant temperatures. Similar aerodynamic conditions must be assumed. They demonstrated the technique in a short-duration

transonic blowdown facility with transient inlet Mach number (initial ramp-up to design condition of 0.88) and mainstream temperature (initial peak followed by a gradual drop off). Test surfaces were made of a low conductivity material so that heat conduction was approximately one-dimensional. Measured surface temperature data (IR thermography) from each of the two tests were used as boundary conditions for a one-dimensional semi-infinite conduction model to reconstruct surface heat flux histories. It was assumed that the two tests (at different coolant temperatures) are conducted at similar aerodynamic conditions, so that η and h could be assumed to be unchanged between tests. At each surface location (pixel), a *dual linear regression technique* was then be used, in which the recovery temperature was incrementally varied to find a minimum difference between the two experiments (at each surface location) in the calculated values of η and h .

For the scaling of metal temperatures (or overall cooling effectiveness, i.e., the conjugate component) in a compressible environment with film cooling, Luque et al. [12,13] demonstrate that conventional definitions of metal effectiveness fail to account for redistribution of heat between regions differently affected by compressibility effects, even when the external recovery factor is accounted for. This is because there is heat redistribution *within the thermal network of the part*, which means a purely local definition of recovery factor is inadequate. The authors show that both the Mach number distribution of the part *and* the thermal network of the part combine to give an *effective local recovery temperature*, which is referred to as the *recovery and redistribution temperature*. The authors show that for results to be independent of mainstream-to-coolant temperature ratio, it is necessary to define metal effectiveness in terms of a recovery and redistribution temperature, T_R , and associated recovery and redistribution parameter $\mathfrak{R} = T_R/T_{01}$. Although the analogy to the conventional theory is obvious, these parameters are entirely distinct from parameters used in previous literature. The authors shown that in an experimental situation, the local value of T_R can only be determined from a series of experiments (at least two) in which the flow field is kept approximately constant, but the mainstream-to-coolant temperature ratio is varied.

Theory

In this section, we introduce the concept of equivalent mainstream effectiveness. The schematic shown in Fig. 1 shows a developing—both spatially and temporally—thermal boundary layer upstream of an ejecting film. In this example, we assume a core-flow temperature (outside the thermal boundary layer, which we take as our reference for the mainstream temperature) at a temperature $T_{01}(t)$, and an upstream wall reference temperature, at a particular location $x = x_1$, $T_{w1}(t)$. Moving away from the wall there is a gradient of temperature between $T_{w1}(t)$ and $T_{01}(t)$. Flow from within the thermal boundary layer is convected downstream. In this process, streamlines at various initial temperatures mix with each other. Flow from these mixing streamlines is then entrained within the partially mixed coolant film, giving rise to a temperature distribution on the surface, $T_w(x, t)$. Here, for simplicity, we refer to incompressible conditions in the mainstream flow.

The resulting wall temperature $T_w(x, t)$ depends on the local mass fraction of coolant gas, η , the temperature of the coolant gas, $T_{02}(t)$, and the mass fractions and associated temperatures of the entrained regions of hot gas that affect the point of interest on the wall. In our framework, we represent the *result* of the hot gas streamlines interacting at a point of interest by an *equivalent mainstream temperature* $T^*(x, t)$ at every point on the surface. In analogy to the adiabatic film effectiveness, we define this temperature in terms of an *equivalent mainstream effectiveness* by

$$T^*(x, t) = \eta^*(x, t)T_{w1}(t) + (1 - \eta^*(x, t))T_{01}(t) \quad (3)$$

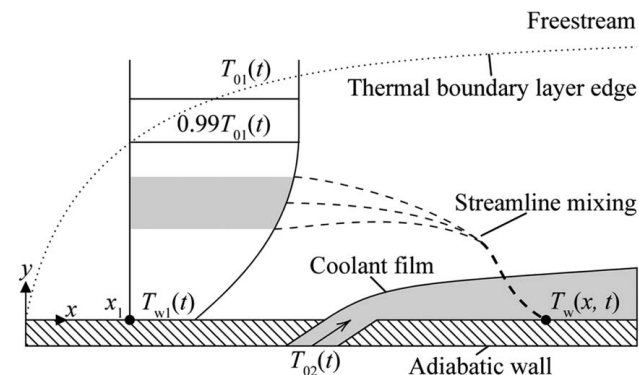


Fig. 1 Schematic of a partially mixed coolant film entraining gas from a (potentially time-varying) thermal boundary layer

where, rearranging for $\eta^*(x, t)$, we get

$$\eta^*(x, t) = \frac{T_{01}(t) - T^*(x, t)}{T_{01}(t) - T_{w1}(t)} \quad (4)$$

Here, $\eta^*(x, t)$ and $1 - \eta^*(x, t)$ can be thought of as the equivalent mass fractions of gas (at the point of interest) at the instantaneous temperature of the upstream wall (at the particular location $x = x_1$), $T_{w1}(t)$, and the instantaneous temperature of the core-flow, $T_{01}(t)$, respectively, that would have had to have mixed to give rise to the equivalent mainstream temperature $T^*(x, t)$ at the point of interest. For completeness we note that although this is a simple way of thinking about it, the analogy is imperfect because the temperature $T^*(x, t)$ arises from the mixing of flow at a range of temperatures between $T_{w1}(t)$ and $T_{01}(t)$. Additionally, we assume that the range of temperature ratio— $T_{01}(t)/T_{w1}(t)$ —over which we are operating is sufficiently small that errors introduced by resulting variation (during the test) of specific heat capacity flux ratio are relatively small and can be ignored. Likewise, we assume that there is little change—across the run—in second-order correction effects associated with, for example, corrections for compressibility.

Having now defined the equivalent mainstream temperature relevant to each point on a surface, $T^*(x, t)$, we are in a position to re-write Eq. (1) replacing the core-flow temperature, $T_{01}(t)$, with the equivalent mainstream temperature $T^*(x, t)$. We defined the *corrected adiabatic film effectiveness*

$$\eta'(x, t) = \frac{T^*(x, t) - T_w(x, t)}{T^*(x, t) - T_{02}(t)} \quad (5)$$

We effectively have two equations—(5) and either (3) or (4)—in two unknowns, $\eta'(x, t)$, and—optionally— $\eta^*(x, t)$ or $T^*(x, t)$. The challenge lies in solving simultaneously for $\eta'(x, t)$ and, say, $\eta^*(x, t)$. This requires at least two sets of data.

Solution of the Equations

Consider an experiment in which the mainstream temperature, $T_{01}(t)$, coolant gas temperature, $T_{02}(t)$, and the upstream wall reference temperature at a particular location $T_{w1}(t)$ are all measured. For simplicity we will assume a set of boundary conditions common in short-duration heat transfer testing, namely, constant coolant supply temperature and mainstream temperature subject to a step change (in time), from the coolant supply temperature to a higher temperature. Thus, in our notation, setting $t=0$ to be the time at which the step change in mainstream temperature occurs, and considering only the period following this step, we can regard both T_{01} and T_{02} as constant and therefore independent of time. It should be noted that this is not a necessary condition for the technique: it is only necessary that the time constant of the upstream surfaces (i.e., the time constant associated with the temperature deficit in the thermal boundary layer) be much greater than the time constant associated with the temperature rise of the mainstream flow.

The idealized experiment is illustrated in Fig. 2 for $\eta^*=0.5$ and $\eta'=0.5$. In an experiment, T_{01} and T_{02} would normally be measured with thermocouple probes, $T_{w1}(t)$ with a wall-mounted thermocouple, and $T_w(x, t)$ with—for example—an infrared (IR) camera.

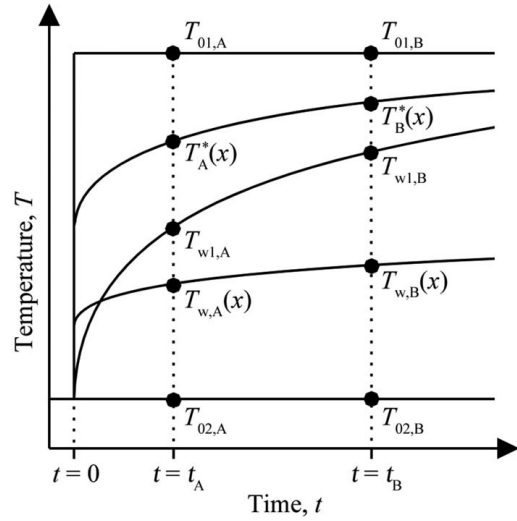


Fig. 2 Example of temperature signals from a single transient run, for $\eta^*=0.5$ and $\eta'=0.5$, with data selected at two evaluation times at $t=t_A$ and $t=t_B$

To solve simultaneously for $\eta'(x, t)$ and $\eta^*(x, t)$ (with corresponding $T^*(x, t)$) we require at least two data points. Timestamps $t=t_A$ and $t=t_B$ are marked in the figure; corresponding measured variables have subscripts A and B for compactness. The characteristics shown are typical for transient heat transfer testing, as demonstrated in “Experimental Demonstration of Technique” section. For an unchanged aerodynamic flow field, and accepting the assumptions stated earlier, we can assume that the following hold true

$$\eta^*(x, t) = \eta_A^*(x) = \eta_B^*(x) \quad (6)$$

$$\eta'(x, t) = \eta_A'(x) = \eta_B'(x) \quad (7)$$

That is, we drop the time dependence in the equations, and equate values of η^* and η' at timestamps A and B. This is equivalent to assuming that the aerodynamic field is unchanged with time between timestamps A and B (same pathlines and mixing) and that the mass fractions (or, more strictly, the specific heat capacity flux fractions) of mixing gas are also constant in time (both $\eta^*(x, t)$ and $\eta'(x, t)$ can be thought of as representing mixing fractions of fluid). Taking these assumptions (i.e., Eqs. (6) and (7)) allows us to solve for η^* and η' as follows. Substituting (5) into (7), we get

$$\frac{T_A^*(x) - T_{w,A}(x)}{T_A^*(x) - T_{02,A}} = \frac{T_B^*(x) - T_{w,B}(x)}{T_B^*(x) - T_{02,B}} \quad (8)$$

Then substituting for $T_A^*(x)$ and $T_B^*(x)$ in (8) using (3), and simplifying using (6), gives Eq. (9), which can be rearranged to give an expression for $\eta^*(x)$, Eq. (10). To explicitly evaluate $T^*(x, t)$ at any time instant, we can substitute $\eta^*(x)$ into (3), and thus, using Eq. (5) we can evaluate $\eta'(x)$

$$\frac{\eta^*(x)T_{w1,A} + (1 - \eta^*(x))T_{01,A} - T_{w,A}(x)}{\eta^*(x)T_{w1,A} + (1 - \eta^*(x))T_{01,A} - T_{02,A}} = \frac{\eta^*(x)T_{w1,B} + (1 - \eta^*(x))T_{01,B} - T_{w,B}(x)}{\eta^*(x)T_{w1,B} + (1 - \eta^*(x))T_{01,B} - T_{02,B}} \quad (9)$$

$$\eta^* = \frac{T_{w,A}(x)(T_{01,B} - T_{02,B}) - T_{w,B}(x)(T_{01,A} - T_{02,A}) + T_{01,A}T_{02,B} - T_{01,B}T_{02,A}}{(T_{01,B} - T_{w1,B})(T_{w,A}(x) - T_{02,A}) - (T_{01,A} - T_{w1,A})(T_{w,B}(x) - T_{02,B})} \quad (10)$$

Experimental Demonstration of Technique

We now demonstrate the proposed technique using experimental data from the Metal Effectiveness Rotor Cooling (MERC) facility [2] at the University of Oxford. The facility is a high-pressure transonic blowdown linear cascade designed to investigate turbine rotor platform cooling. A modular working section allows rapid interchangeability of blades and the study of both metal and plastic parts. For the data presented in this paper, the facility was configured to measure the adiabatic film effectiveness arising from leakage flows from hub seals. To do this, very low conductivity parts were used.

Facility Overview and Instrumentation. For the tests described, the modular working section was built with a linear cascade of rotor blades manufactured from glass-filled (GF) nylon. The blades included platform, shank and fir-tree root, to ensure representative flow in the cavity beneath the blades. The platforms are cooled with leakage flows both at the rotor-stator interface, and the so-called *slashface* between pairs of rotor blades. This is shown schematically in Fig. 3.

During experiments, the mainstream flow is heated using a fast-response heater mesh (~ 150 kW power) giving a near step change (in time) in mainstream temperature of 53 K and a corresponding mainstream-to-coolant temperature ratio of approximately 1.2 which is stable throughout the heated period. A typical core-flow temperature trace $T_{01}(t)$ is shown in Fig. 4. In this run, the heater is turned on at approximately 40 s, and turned off at approximately 70 s. The temperature spike at approximately 10 s is associated with the initiation of flow and pressurization of the facility. The core-flow temperature was measured using five thermocouple rakes, each with 6 K-type bare-bead thermocouples (wire diameter 0.13 mm; approximate time constant, $\tau = 0.15$ s). These are shown in Fig. 3. The core-flow temperature rise has a *measured* time constant of approximately 0.17 s; this is very close to the thermocouple time constant and the true time constant is likely lower (a theoretical estimate gives 0.01 s).

The upstream wall reference temperature, $T_{w1}(t)$, was measured using an assembly comprising a 0.5 mm thick copper disk 5 mm in diameter, an underside K-type thermocouple, and a 1 mm thick insulating layer of rigid foam (Rohacell; $k = 0.03$ W/(m K)). The purpose of the assembly is to register an accurate wall gas temperature measurement independent of the heat flux into the surrounding conducting surface: the assembly is essentially adiabatic. The time constant of the assembly is estimated to be 0.15 s. The location and

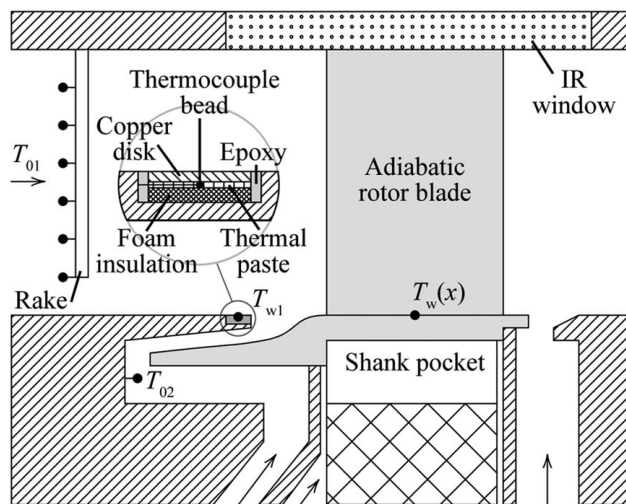


Fig. 3 Schematic cross section of the linear cascade working section showing the locations of measurements: $T_{01}(t)$, the core-flow; $T_{w1}(t)$, the upstream wall reference temperature; $T_{02}(t)$, the coolant flow; $T_w(x, t)$, the platform surface

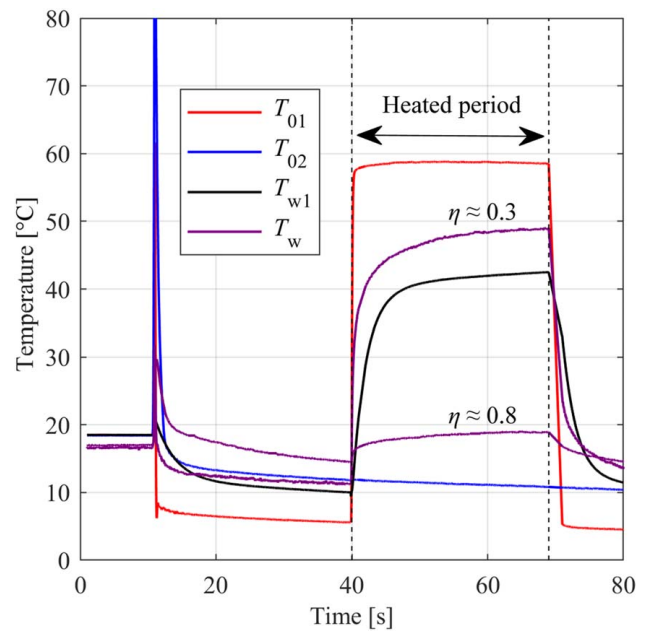


Fig. 4 Typical experimental temperature traces for the core-flow temperature, $T_{01}(t)$; the upstream wall reference temperature, $T_{w1}(t)$; the coolant temperature, $T_{02}(t)$; and the platform surface temperature, $T_w(x, t)$ at two locations with $\eta \approx 0.8$ and $\eta \approx 0.3$

construction of the measurement system is shown in Fig. 3. Further details of the technique, and the corresponding uncertainty analysis, are reported in Ref. [14].

A typical response of the upstream wall reference temperature, $T_{w1}(t)$, is shown in Fig. 4. The time constant of this trend is approximately 2.5 s. The time constants of the inlet components are those for approximately 50 mm thick aluminum surfaces: in the range 150–300 s for heat transfer coefficients in the range 500–1000 W/(m² K). The time constant of the upstream wall reference temperature is related both to the time constant of the inlet components and the boundary layer flow (related to the transit time of gas between the heater and the inlet section). The downstream adiabatic surfaces— $T_w(x, t)$ in Fig. 4—respond to the core-flow temperature, having similar time constants. This makes evaluating the adiabatic effectiveness very challenging by means of conventional processing techniques. The problem is overcome with the method proposed in this paper.

Coolant outlets are supplied by a common plenum, in which the gas temperatures are measured using K-type thermocouples close to the cavity exit. These are shown in Fig. 3. The coolant feed temperature and initial temperature of the facility walls are both approximately at ambient conditions, so the individual coolant outlet temperatures are very similar to each other, and vary little with time. A typical coolant temperature characteristic, $T_{02}(t)$, is shown in Fig. 4.

The platform surface temperature distribution, $T_w(x, t)$, was measured using a calibrated IR camera system. Typical traces from locations with low ($\eta' \approx 0.3$) and high ($\eta' \approx 0.8$) effectiveness regions are shown in Fig. 4.

Measurements were averaged over 5×5 pixels regions. The blades are manufactured from glass-filled nylon, which has low thermal conductivity (0.25–0.30 W/(m K)). The platforms were approximately 5 mm thick, rendering them effectively thermally semi-infinite. For an estimated average heat transfer coefficient of 1200 W/(m² K), the time constant of the surface of interest was estimated to be 0.58 s. This value is in good agreement with the values of 0.41 s and 0.76 s for the sample regions reported in Fig. 4. Small differences in time constant arise due to local variations in heat transfer coefficient across the surface.

To further illustrate the severity of the processing problem to be overcome, we plot in Fig. 5 the ratio of the core-flow temperature,

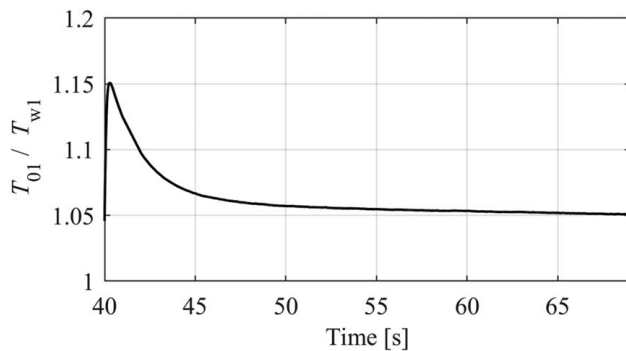


Fig. 5 Ratio of the core-flow temperature, $T_{01}(t)$, and the upstream wall reference temperature, $T_{w1}(t)$, as a function of time

$T_{01}(t)$, and upstream wall reference temperature, $T_{w1}(t)$, as a function of time. Just after the heater is initiated (~ 40 s) this ratio is approximately 1.15. In the first 5 s, this decreases to 1.07. Toward the end of the heated period (~ 69 s), the ratio reaches 1.05, decaying only very slowly. It is clear that to reach a value of unity would take an impractically long time, beyond the scope of most semi-transient test facilities (common for transonic testing).

In Fig. 6, we show a typical spanwise temperature profile at cascade inlet (for location, see Fig. 3) evaluated for the run shown in Fig. 4, at a time instant just before the heater is turned off (~ 69 s), using a single thermocouple rake. The hub wall measurement (span fraction of zero) was performed with the adiabatic wall measurement system. Although the spanwise resolution is relatively coarse, the thermal boundary layer can be estimated to extend to a span fraction of approximately 0.2 from either endwall. The central four thermocouples (on each of the 5 probes) read very similar temperatures allowing the core-flow temperature to be accurately established.

Application of the Proposed Method. In the presence of an inlet thermal boundary layer, and with a complex aerodynamic field between the inlet measurement plane and the surface of interest, adiabatic film effectiveness distributions evaluated using conventional methods are difficult to interpret on account of arbitrariness in the selection of the hot gas temperature. This makes the film effectiveness data impossible to transport between environments, e.g., to infer an engine condition, or to compare to other experimental data. The technique proposed in this paper is designed to correct the film effectiveness data to the values one would have expected in the absence of an inlet thermal boundary layer.

In this section, we take full-surface film effectiveness measurements for a rotor blade platform, and process the data using the conventional method, and the proposed method. We will see that the conventional method delivers unrealistic—and in certain regions nonphysical—results, which are not time-independent. That is,

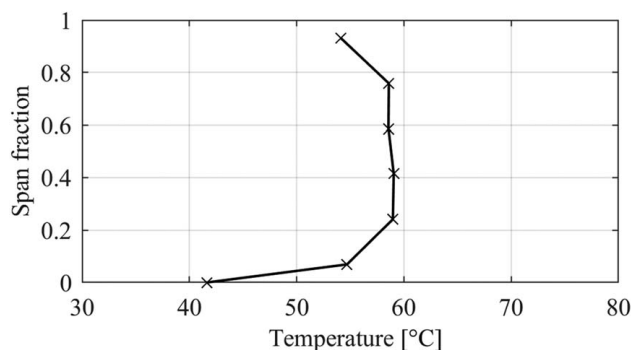


Fig. 6 Spanwise inlet temperature evaluated at ~ 69 s for the run shown in Fig. 4

the results depend on the time-varying state of the inlet thermal boundary layer. We then see that the proposed method renders the results independent of time and corrects nonphysical values.

Conventional Technique. For comparison with the proposed technique, we first process the data using the conventional method. We arbitrarily define the hot gas temperature, $T_{01}(t)$, as the mean of all the inlet thermocouples. The resulting adiabatic film effectiveness distribution for the run shown in Fig. 4 is shown in Fig. 7.

The evaluation time was 69 s, at the end of the heated period immediately prior to the heater being switched off. The distribution shows good detail. The low-effectiveness strip along the bottom of the image is an aluminum overhang which forms the stator-side of the front rim seal structure and overlaps the front of the blade—this is relatively cool on account of it being highly nonadiabatic. On the same strip, we can see two half-circles (C and D) which mark the copper disks for measurement of $T_{w1}(t)$. On these adiabatic patches, the measured value of η is approximately 0.30. This is non-physical because there is no upstream coolant ejection (a value of $\eta = 0$ is expected). The dominant features on the main body of the platform are as follows: a well-cooled leading region of the platform; the sweeping of coolant toward the suction surface, caused by the passage crossflow [15]; the introduction of a secondary cooling film toward the rear of the platform as coolant leaks through the blade slashface from the internal cavity; a wedge-shaped region of low effectiveness caused by the trailing edge wake.

To illustrate the difficulty of interpreting the data processed in this way, and also the time-dependent nature of the problem, we take the average value of η in regions C, D, E, and F in Fig. 7, and plot the trends $\eta(t)$ during the heated period of the run. These trends are shown in Fig. 8. E and F mark arbitrary regions of relatively high and relatively low effectiveness, respectively, on the main body of the platform.

We now examine the trends of $\eta(t)$ from regions C, D, E, and F, shown in Fig. 8. The data are plotted as a function of the fraction of the time representing the heated period of the run. Regions C and D mark—approximately adiabatic—surface measurement patches, which are upstream of the cooling flow, and should, therefore, have a cooling effectiveness of zero. Although there is good agreement between the two readings, using the conventional processing technique, the reported values of $\eta(t)$ are both nonphysical (between 0.79 and 0.33, as opposed to zero) and strongly varying in time. E and F mark arbitrary regions of relatively high and relatively low

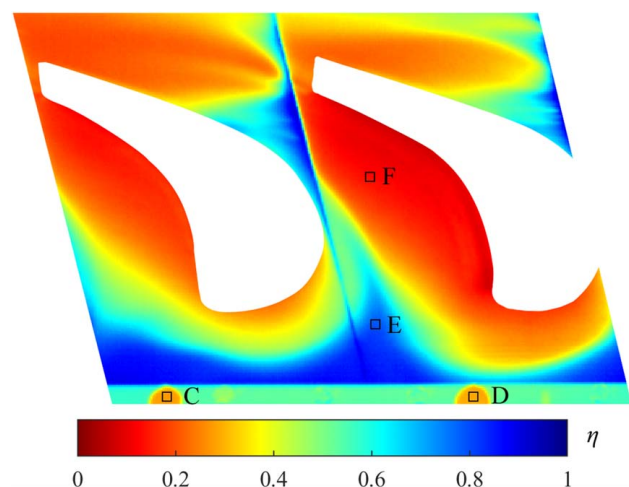


Fig. 7 Adiabatic film effectiveness distribution processed using the conventional technique, with $T_{01}(t)$ defined as the mean inlet temperature. C and D mark approximately adiabatic copper disks associated with the wall temperature measurement system. E and F mark arbitrary regions of relatively high and relatively low effectiveness, respectively, on the main body of the platform.

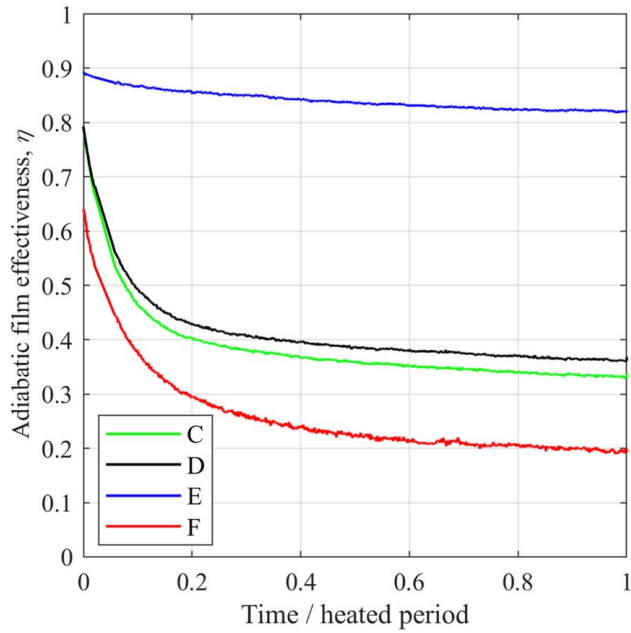


Fig. 8 Trends of $\eta(t)$ from regions B, C, D, and E in Fig. 7, using a conventional processing technique with $T_{01}(t)$ defined as the mean inlet temperature. Here, $\eta(t)$ is defined according to Eq. (1).

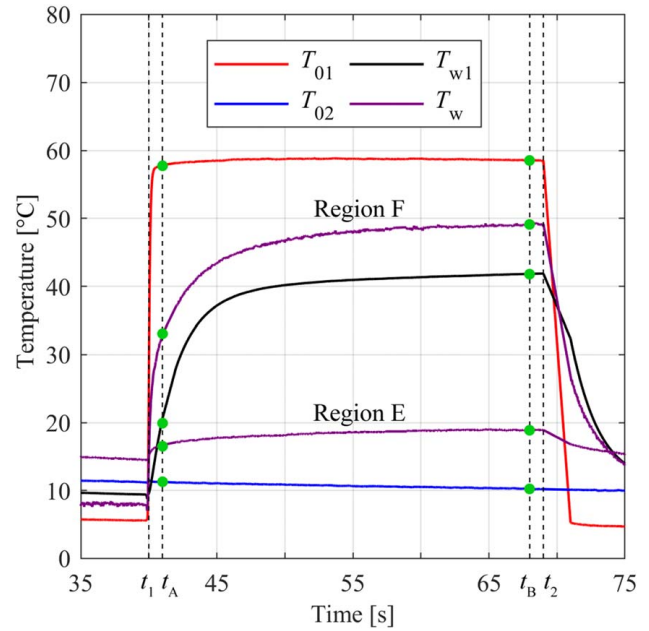


Fig. 9 Data from the heated period of a run ($t_1 \leq t \leq t_2$) showing particular timestamps $t_A = 41.0$ s and $t_B = 68.0$ s, or $t'_A = 0.038$ and $t'_B = 0.97$. Wall temperatures, $T_w(t)$, in regions E and F (see Fig. 7) are also marked.

effectiveness on the main body of the platform. At location E, there is less variation of $\eta(t)$ with time because $T_w(t)$ is dominated by the coolant flow temperature, $T_{02}(t)$, and is therefore insensitive to both the variation in and ambiguity in the definition of $T_{01}(t)$. At F the reverse is true. In this low-effectiveness region, there is significant dependence on $T_{01}(t)$, and the strongly time-varying trend (despite the surface being near-adiabatic) clearly demonstrates the problem in definition of $\eta(t)$. Even the settled value at F, of $\eta \approx 0.3$ is physically unlikely, because this is behind the separation line marked by the horseshoe vortex and is typically completely starved of cooling flow (and effectiveness of zero is expected).

Proposed Technique. We now process the same data using the proposed technique in which we simultaneously solve for η^* and η' by using data from a number of timestamps during the run. In the first instance we use two timestamps to show the simplest implementation of the technique.

The data of Fig. 4 are reproduced in Fig. 9 for the time period 35 s to 75 s. As an example of the local temperature trends the average temperatures in regions E and F are also shown. The heated period is $t_1 = 39.9$ s to $t_2 = 69.0$ s, a duration of 29.1 s. For comparison with other timestamp combinations, we define a nondimensional time by

$$t' = \frac{t - t_1}{t_2 - t_1} \quad (11)$$

In the current processing, we use timestamps at $t_A = 41.0$ s and $t_B = 68.0$ s, or $t'_A = 0.038$ and $t'_B = 0.97$. These are somewhat arbitrary timestamps chosen to give a substantial difference between the two data. We examine the sensitivity to choice of time-step in a later section. The times t_1 , t_2 , t_A , and t_B are marked in Fig. 4.

Solving simultaneously for η^* and η' across the full surface of the vane, using data at each pixel location of the type given in Fig. 9, at timestamps $t'_A = 0.038$ and $t'_B = 0.97$, gives the distributions of η^* and η' presented in Fig. 10. The method used for solution is that presented in the section above entitled *solution of the equations*.

We first examine the resulting corrected adiabatic film effectiveness, η' (Fig. 10(a)). Using the new processing technique, the

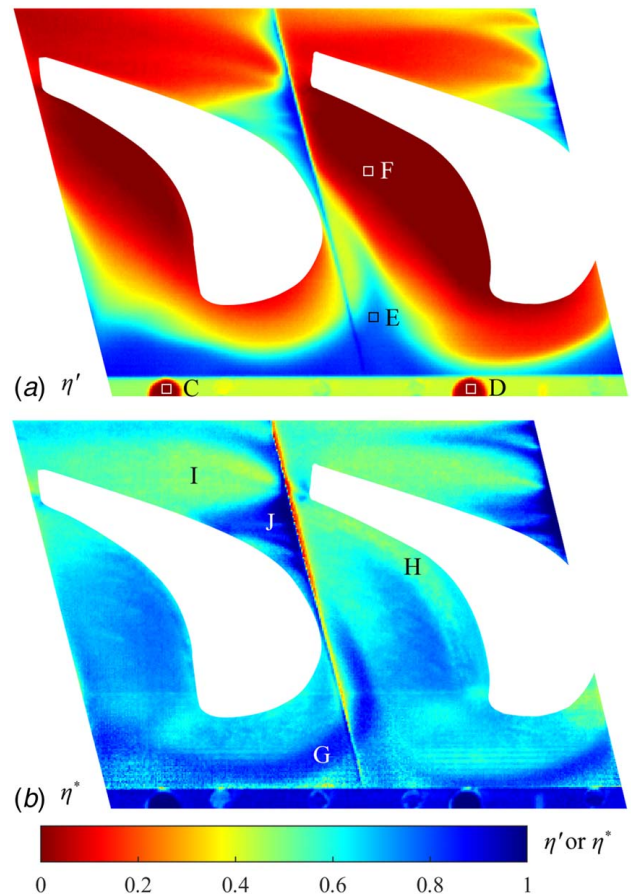


Fig. 10 (a) Adiabatic film effectiveness distribution of two turbine rotor blade platforms, calculated using the proposed methodology and (b) corresponding equivalent mainstream effectiveness distributions

approximately adiabatic copper patches have an effectiveness close to zero, as expected; we recall that in the conventional processing technique, values between 0.79 and 0.33 were returned, which were nonphysical. Likewise, in the region behind the horseshoe vortex, close to the suction side of the vane, a wide region of close to zero effectiveness is observed. This is in-line with expectation because the region behind the horseshoe vortex is typically entirely starved of coolant flow. The leading region of the platform, directly downstream of the coolant ejection, and the region downstream of the slashface deeper into the passage have high values of corrected adiabatic film effectiveness ($\eta' > 0.8$) consistent with expectation.

Overall, the distribution of η' is similar to the distribution of η achieved using a mean inlet temperature for $T_{01}(t)$, but values have been corrected downward. This is to be expected if the choice of mean inlet temperature for $T_{01}(t)$ in the conventional definition of η was unrepresentatively high compared with the actual mainstream fluid temperatures entrained within the mixing cooling layer. As the temperature deficit in the inlet thermal boundary layer is—by definition—concentrated toward the endwalls, it is natural that choice of mean inlet temperature for $T_{01}(t)$ would generally be an overestimate of the temperature of the entrained gas, and a correction to lower values ($\eta' < \eta$) is expected.

We now briefly examine the distribution of equivalent mainstream effectiveness η^* , presented in Fig. 10(b): our purpose here is not to explain the flow structure in detail, but simply to demonstrate the reasonableness of the profile.

On the approximately adiabatic copper disks (region C, D), the value of η^* is by definition unity. A crescent of high equivalent mainstream effectiveness (region G) can be seen upstream of and wrapping around the leading edge of the blade. Here, we have $\eta^* \sim 0.9$. Upstream of this crescent, the lower inlet boundary layer fluid is forced over the coolant flow (leading region of high η' in Fig. 10(a)), leading to stratification of the flows. Where the horseshoe vortex forms, at the position of the crescent, this lower boundary layer fluid is rolled down into the coolant flow, mixing for the first time. Thus, high values of η^* (representing fluid close to the temperature $T_{w1}(t)$) are expected in this region.

Region H, along the pressure side (PS) fillet of the blade, has low values of η^* (in the range $0.5 < \eta^* < 0.6$). This is to be expected due to the downwash from the PS of the vane, as low-momentum boundary layer fluid is drawn across the passage (from PS to SS) by the cross-passage pressure gradient. As flow is drawn down the blade it is replaced by fluid from regions of higher span, corresponding to higher temperature and lower values of η^* . Likewise the late SS region, and the region downstream of the trailing edge (marked I) there is a large region of low η^* (in the range $0.4 < \eta^* < 0.6$). Here, the flow is highly mixed in the spanwise direction, due to both large-scale vortices rolling into the SS corner and off the trailing edge of the blade, and due to turbulence generated by trailing edge shedding.

Region J has higher values of η^* (in the range $0.7 < \eta^* < 1.0$) than might be physically expected. Although this points to instability in the technique, the resulting values of η' are relatively insensitive to η^* , η' taking values close to unity in this region because the near-wall flow is dominated by coolant flow leaking through the slashface gap.

To look quantitatively both at the correction η to η' , and to look at the physical reasonableness of the values of η^* , we plot histograms of percentage of pixels falling in *buckets* of values for both the conventional and proposed technique. The same data as presented in Figs. 7 and 10 was used for these images, but the strip extending between and beyond C and D was removed, because this surface is nonadiabatic. The histograms are shown in Fig. 11. The correction η to η' acts to lower the mean value of effectiveness, with the correction being greater at low values of η than at high values. Lowering the values is expected on account of the average temperature of entrained mainstream gas being overestimated in our implementation of the conventional method. A greater correction at low values of η is expected because in this range the value of η is more sensitive to the temperature of entrained gas.

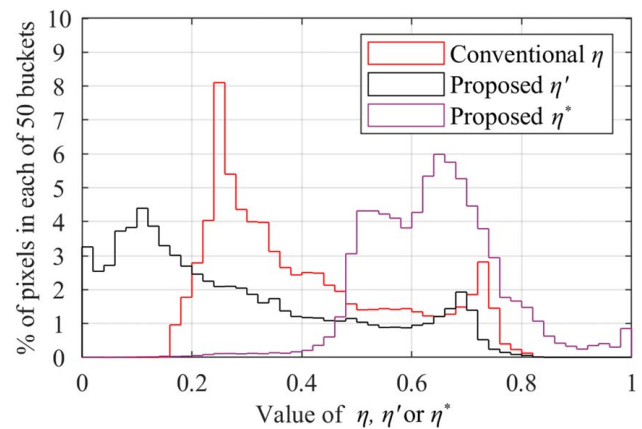


Fig. 11 Histograms of percentage pixel counts in each of 50 equal buckets for conventional adiabatic film effectiveness, η ; corrected adiabatic film effectiveness, η' ; and equivalent mainstream effectiveness, η^*

The uncorrected distribution of η has no values below 0.18, which—alone—suggests an offset error, the cause of which has been discussed. The corrected values η' extend all the way to zero, giving physically reasonable values in regions where no coolant can reach the surface (as predicted by computational fluid dynamics (CFD)).

The distribution η^* has most of its weight between $0.5 < \eta^* < 0.7$, with only small tails at high and low values of η^* . Examining Fig. 6, which shows the thermal boundary layer extending to approximately 20% span, and noting the typical secondary flow patterns and spanwise length scale of flow structures for high-turning blades, this range of η^* is thought to be reasonable. The absence of significant weight in the range $0.7 < \eta^* < 1.0$ is explained by the fact that the thermal boundary layer is forced over the coolant flow in the leading part of the passage, and first interacts with the wall only as it rolls into the horseshow vortex, a process that necessitates moderate mixing. The absence of significant weight in the range $0.0 < \eta^* < 0.5$ is explained by the depth of the thermal boundary layer, and the fact that we are studying only the endwall: that no core-flow, unmixed with fluid from within the thermal boundary layer, interacts with the endwall is unsurprising as it would require spanwise migration of more than 20%.

Stability of the Process. The aim of the proposed technique is to avoid the sensitivity of the conventional adiabatic film effectiveness, η , to variation with time of the nondimensional temperature in the inlet thermal boundary layer. In the proposed method, corrected adiabatic film effectiveness, η' , should be independent of time. More precisely perhaps, because the technique relies on the use of at least two timestamps, the value of η' returned should be independent of the choice of timestamps.

In the foregoing analysis, the timestamps A and B were chosen somewhat arbitrarily, but respecting the rather obvious condition that greater sensitivity is achieved by choosing times that allow for significant change in the *absolute* temperature of the boundary layer fluid. This is a stability requirement for solution of Eqs. (9) and (10).

To understand the sensitivity to timestamp selection, we calculate η' for every possible pair of timestamps (t'_A and t'_B) taken from the heated period of the run. Results are shown in Fig. 12 for region E in Fig. 7.

In the range $0.020 < t'_A < 0.10$ (early start time) and $0.4 < t'_B$ (sufficiently long separation in time to ensure good thermal rise), the value of η' returned is relatively insensitive to timestamp selection, varying between 0.75 and 0.81. For a method using only two timestamps, it is recommended to choose values within this region. For reference, we note that the range $0.020 < t'_A < 0.10$ (or $0.58 < t_A < 2.9$ s) is equivalent to between 0.23 and 1.2 time

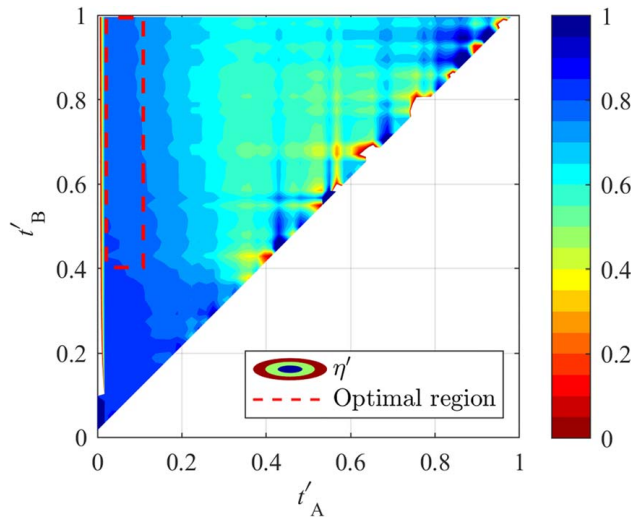


Fig. 12 Value of η' returned by the proposed method for region E for every combination of timestamps t'_A and t'_B

constants for the inlet thermal boundary layer ($\tau=2.5$ s) and between 1.0 and 5.0 time constants of the surface of interest ($\tau=0.58$ s).

As expected, close to the line $t'_B = t'_A$ the solution becomes unstable, because the temperatures $T_{w1,A}$ and $T_{w1,B}$ are close in value. Likewise, as t'_A increases in region $t'_A > 0.20$, there is significant sensitivity to the timestamp pair due to reducing temperature difference between the two timestamps. At the very start of the experiment, $0 < t'_A < 0.020$, the solution is unstable as $T_{w1,A}$ is very close in value to that of the coolant, T_{02} : a separation in values between $T_{w1,A}$ and T_{02} is required in order to distinguish coolant gas from low temperature gas in the mainstream.

Uncertainty With Two Timestamps

In this section, we perform an uncertainty analysis for the proposed method applied with two timestamps within the heated period. Timestamps are taken from near the end of a run, and within the first two seconds of the heated period. To make the results as generically applicable as possible, we take nominal ranges for parameters that are representative of typical well-conditioned laboratory experiments, not unlike the experiment of this study. The purpose is to calculate confidence limits in η' and to guide best-practice in application of the proposed technique.

We consider the impact on uncertainty in η' of mainstream-to-coolant temperature ratio, T_{01}/T_{02} ; ratio of upstream wall reference temperature between timestamps, $T_{w1,A}/T_{w1,B}$; and equivalent mainstream effectiveness, η^* . Ranges for each parameter and corresponding estimated uncertainties are presented in Table 1. For this analysis, coolant is assumed to be air at room temperature. Core-flow temperature is defined by the ratio T_{01}/T_{02} and is taken as a fixed value for both timestamps. The upstream wall reference temperature, T_{w1} , varies between T_{02} and T_{01} . Surface wall temperature, T_w , is derived from values of η' and η^* covering the range 0–1.

Measurements taken with thermocouples are assumed to have been normalized at an isothermal condition (normally settling to ambient temperature) and recorded at sufficiently high sampling rate that precision uncertainty in the running (down-sampled) mean becomes negligible. The uncertainty is therefore dominated by bias caused by cold junction compensation drift, differences in individual thermocouple calibrations that are not accounted for, and by nonlinearity and hysteresis in the particular thermocouple calibration taken. Some of these terms can be taken as having a fixed uncertainty (strictly, uncertainty distribution) and others should properly be considered to have a distribution that is

Table 1 Assumed temperature ranges and corresponding estimated absolute uncertainties (to 95% confidence)

Parameter	Units	Value	U (K) 95%	Source
T_{01}	K	293–440	± 0.5	K-type thermocouple
T_{02}	K	293	± 0.5	K-type thermocouple
T_{01}/T_{02}	–	1–1.5	–	Calculated
T_w	K	293–440	± 1.0	IR camera
T_{w1}	K	293–440	± 0.5	K-type thermocouple
$T_{w1,A}/T_{w1,B}$	–	0.7–1.0	–	Derived

proportional to the temperature offset from the normalization point. Because of the relative complexity of implementing such a distribution, we instead take an estimated upper bound on the uncertainty (i.e., that at the maximum temperature condition) as applicable to the entire temperature range. This upper bound is taken to be ± 0.5 K to 95% confidence. For measurements taken with two (or more) thermocouples, we do not consider the measurements sufficiently independent to perform a $1/\sqrt{2}$ —or greater—reduction, and retain the ± 0.5 K uncertainty limits.

The uncertainty in T_w was taken as ± 1.0 K to 95% confidence, representative of a laboratory-calibrated IR camera setup [16]. This is the combined overall uncertainty including contributions arising from uncertainty in target surface emissivity, window transmissivity, reflected surrounding radiance, and black body calibration uncertainty.

Expected uncertainties in η' have been calculated by the root-sum-squared (RSS) method. This uses the partial derivatives of the functions used to calculate η^* and η' (Eqs. (5) and (10)) with respect to each input temperature and the associated measurement uncertainty.

Effect of Mainstream-to-Coolant Temperature Ratio. We first consider the effect of mainstream-to-coolant temperature ratio on the absolute overall uncertainty in η' (i.e., expressed as $\eta' \pm U_{\eta'}$). We define an example case, using values from Table 1, in which T_{02} is fixed at 293 K and T_{01}/T_{02} is varied between 1.0 and 1.5. We define a surface temperature near the start of the heated period as $T_{w1,A} = 0.67(T_{01} - T_{02}) + T_{02}$, and a surface temperature near the end of the heated period as $T_{w1,B} = 0.90(T_{01} - T_{02}) + T_{02}$. These expressions are selected to give optimal timestamps for a two-timestamp method, as discussed in the Effect of timestamp selection section. For a system in which the mainstream, coolant, and upstream wall reference all start at the same temperature, and in which the coolant temperature is constant during the experiment, the upstream wall reference temperature at any subsequent moment in time will have a temperature offset from the coolant proportional to the temperature difference ($T_{01} - T_{02}$). If the time constants of the system are independent of T_{01}/T_{02} (same aerodynamic field), the expressions for $T_{w1,A}$ and $T_{w1,B}$ above reference the same points in time (i.e., the upstream wall reference temperature trends are scaled versions of each other).

Using these values, we calculate the overall uncertainty in corrected adiabatic film effectiveness, η' , as a function of η' and T_{01}/T_{02} . The result is plotted in Fig. 13 for $\eta^* = 0.90$ (the impact of η^* on $U_{\eta'}$ is discussed in a later section).

The uncertainty in η' is low when the temperature ratio is high (between 0.050 and 0.052 for a typical laboratory temperature ratio of $T_{01}/T_{02} = 1.2$ —red line on Fig. 13—like the current experiment), but increases somewhat exponentially as the temperature ratio approaches unity ($T_{01}/T_{02} = 1.0$). The uncertainty in η' is above 0.10 for $T_{01}/T_{02} < 1.1$, marking a practical lower limit of temperature ratio that would need to be achieved for acceptable uncertainty. This would correspond to mainstream heating of approximately 28 K in typical laboratory experiments ($T_{02} = 290$ K). The uncertainty in η' is only very weakly dependent on the absolute value of η' .

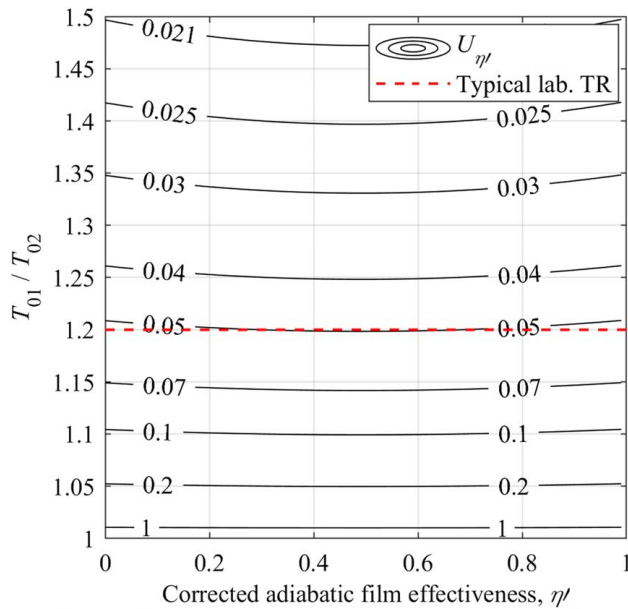


Fig. 13 Contours of absolute overall uncertainty in η' as a function of η' and T_{01}/T_{02} for $T_{w1,B} = 0.90(T_{01} - T_{02}) + T_{02}$, $T_{w1,A} = 0.67(T_{01} - T_{02}) + T_{02}$ and $\eta^* = 0.90$

Effect of Timestamp Selection. We now consider the effect of timestamp selection, by considering the absolute overall uncertainty in η' as a function of the ratio of the upstream wall reference temperatures evaluated at timestamps A and B, $T_{w1,A}/T_{w1,B}$. For a given characteristic response, this ratio can be considered a proxy for the times at which the two data are taken. Somewhat arbitrarily, we take $T_{01}/T_{02} = 1.5$ and $T_{w1,B} = 0.90(T_{01} - T_{02}) + T_{02}$. This represents an experiment with significant mainstream heating (e.g., by approximately 150 K from ambient to an absolute temperature of 440 K) and an—assumed—near-end-of-heated-period condition with moderate inlet boundary layer temperature nonuniformity

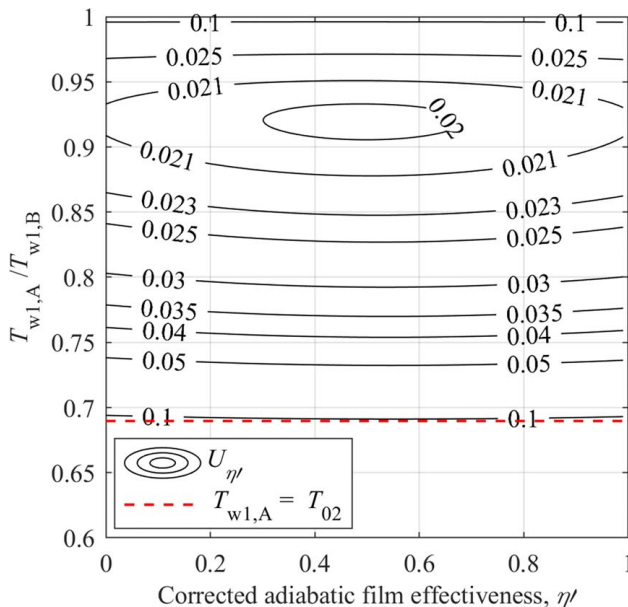


Fig. 14 Contours of absolute overall uncertainty in η' as a function of η' and $T_{w1,A}/T_{w1,B}$ for $T_{w1,B} = 0.90(T_{01} - T_{02}) + T_{02}$, $T_{01}/T_{02} = 1.5$; and $\eta^* = 0.90$

(approximately 15 K across the boundary layer). We then vary $T_{w1,A}/T_{w1,B}$ in the range $0.68 < T_{w1,A}/T_{w1,B} < 1.00$ (where the lower limit represents $T_{w1,A} = T_{02}$, and the upper limit represents timestamps very close together in time) and examine the impact on the absolute overall uncertainty in η' , $U_{\eta'}$. Results are shown in Fig. 14 for $\eta^* = 0.90$ (flow from lower regions of the thermal boundary layer, i.e., close to the upstream wall reference temperature, T_{w1})

As expected, in the approach to the upper and lower limits ($T_{w1,A}/T_{w1,B} = 1.00$ and $T_{w1,A}/T_{w1,B} = 0.68$, respectively), the uncertainty in η' increases somewhat exponentially. At the upper limit, there is—by definition—no temperature difference between the timestamps (taken at the same time) and therefore the solution of Eqs. (5) and (10) is extremely unstable. At the lower limit, there is no temperature difference between the measured upstream wall reference temperature at the first timestamp, $T_{w1,A}$, and the coolant temperature, T_{02} , making it difficult to separate contributions from lower boundary layer fluid and coolant.

For $\eta^* > 0.9$ (not shown; equivalent mainstream temperature closer to the upstream wall reference temperature), both the uncertainty and the gradient of uncertainty in η' are higher in the approach to the lower boundary ($T_{w1,A} = T_{02}$) than in the example represented by Fig. 14. In the limit of the equivalent mainstream effectiveness approaching unity, $\eta^* \rightarrow 1$, corresponding to the entrained fluid coming from the bottom of the inlet thermal boundary layer, the equivalent mainstream temperature approaches the upstream wall reference temperature, $T^* \rightarrow T_{w1}$. At the start of the heated period, where the upstream wall reference temperature is close to that of the coolant, $T_{w1} \approx T_{02}$, this would result in the equivalent mainstream temperature also being close to that of the coolant ($T^* \approx T_{02}$). In this limit, the temperature difference $T^* - T_{02}$ is small, and hence Eq. (5) becomes unstable as the denominator approaches zero.

For our particular reference values, there is a fairly broad region of low uncertainty in η' (below 0.025) in the range $0.85 < T_{w1,A}/T_{w1,B} < 0.96$, with an optimum at $T_{w1,A}/T_{w1,B} \approx 0.92$ (the condition chosen for preceding section: “Effect of mainstream-to-coolant temperature ratio.”). This result is relatively independent of the value of η' but with a shallow minimum in the range $0.30 < \eta' < 0.70$.

Perhaps expectedly, the conclusion is that timestamps should be selected such that there is a large difference between both $T_{w1,A}$ and $T_{w1,B}$ and between T_{w1} and T_{02} . One way of thinking about this is the following: in the proposed technique while it is still necessary to maintain a temperature difference between the mainstream gas temperatures and coolant (the minimum difference being dictated by the upstream wall reference temperature) to allow film effectiveness to be determined with acceptably low uncertainty, it is additionally the *change* in upstream wall reference temperature ($T_{w1,A}$ to $T_{w1,B}$) that allows the equivalent mainstream effectiveness to be simultaneously determined.

Effect of Value of Equivalent Mainstream Effectiveness. The equivalent mainstream effectiveness, η^* , is a function of the inlet thermal boundary layer profile and the flow pattern. While it is hard to imagine a situation in which it could be preferentially controlled, it is nonetheless interesting to consider the impact of the value of η^* on uncertainty in η' . This result is plotted in Fig. 15 for $T_{01}/T_{02} = 1.50$, $T_{w1,B} = 0.90(T_{01} - T_{02}) + T_{02}$, and $T_{w1,A}/T_{w1,B} = 0.92$ (an optimum value for this condition, as shown in the Effect of timestamp selection section). The result is that the uncertainty in η' has a relatively weak sensitivity to the value of η^* , varying by a maximum of approximately 22% (for $\eta' = 0.50$) in the range $0 < \eta^* < 1.00$.

This example also shows us that in a well-conditioned and optimized experiment (i.e., for the nominal values above), the proposed technique allows very low uncertainty (below 0.022) in corrected film effectiveness, even for the case of significant inlet thermal boundary layers.

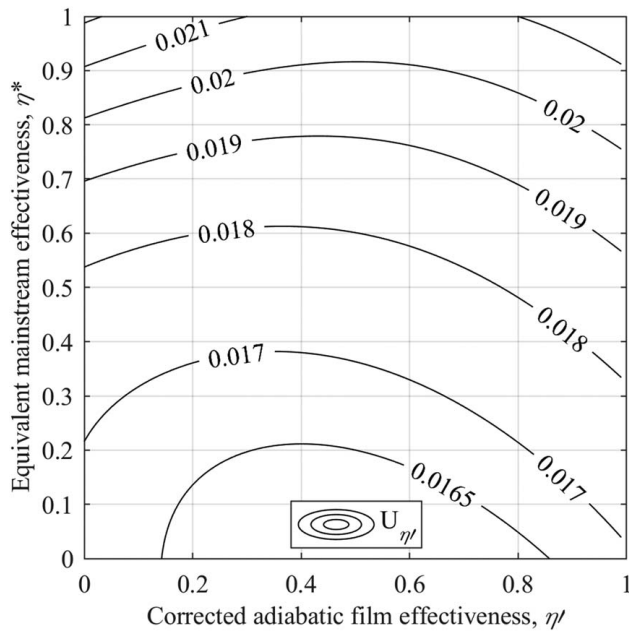


Fig. 15 Contours of absolute overall uncertainty in η' as a function of η' and η^* for $T_{01}/T_{02} = 1.50$, $T_{w1,B} = 0.90(T_{01} - T_{02}) + T_{02}$, and $T_{w1,A}/T_{w1,B} = 0.92$

Method to Reduce Uncertainty by Using Multiple Timestamps

In the Effect of value of equivalent mainstream effectiveness section, we calculated the expected overall uncertainty in η' when two timestamps were used. In this section, we demonstrate that it is possible to reduce uncertainty in η' by taking a larger number of timestamps ($N > 2$) during the heated period of the run, $0 < t' < 1$. For simplicity, we limit ourselves to timestamps evenly distributed between the start and end of the heated period.

The principle is to take every possible pair of timestamps (expressed as a binomial coefficient (N choose 2)), from the set N , and for each calculate values of η^* and η' , and associated uncertainties (using the RSS method, as above). A *weighted-average* value of η' is then calculated by taking a weighted sum according to Eq. (12), where we weight by the square of the inverse of the uncertainty value. This gives low weight to high uncertainty pairs, and high weight to low uncertainty pairs

$$\bar{\eta'} = \frac{\sum_i \binom{N}{2} \eta'_i \left(\frac{1}{U_{\eta'_i}} \right)^2}{\sum_i \binom{N}{2} \left(\frac{1}{U_{\eta'_i}} \right)^2} \quad (12)$$

A Monte Carlo analysis was performed using 1000 virtual experiments based on an idealized virtual experiment with similar physical conditions to the real data presented in Fig. 9. The *idealized* virtual experiment (the initial experiment) is shown in Fig. 16 and has duration of 30 s, similar to the heated period of the experiment of Fig. 9. This is similar to the physical conditions of the real experiment but with T_{01}/T_{02} set to a constant value of 1.20, and T_{w1} derived analytically from the response of a semi-infinite surface with physical properties typical of aluminum and a surface heat transfer coefficient contrived to match the measured thermal boundary layer time constant of 2.5 s and measured temperature value $T_{w1} = 316$ K at $t' = 1$. The constant value $\eta^* = 0.5$ was used, with T^* calculated from Eq. (3). Three surface temperature traces were

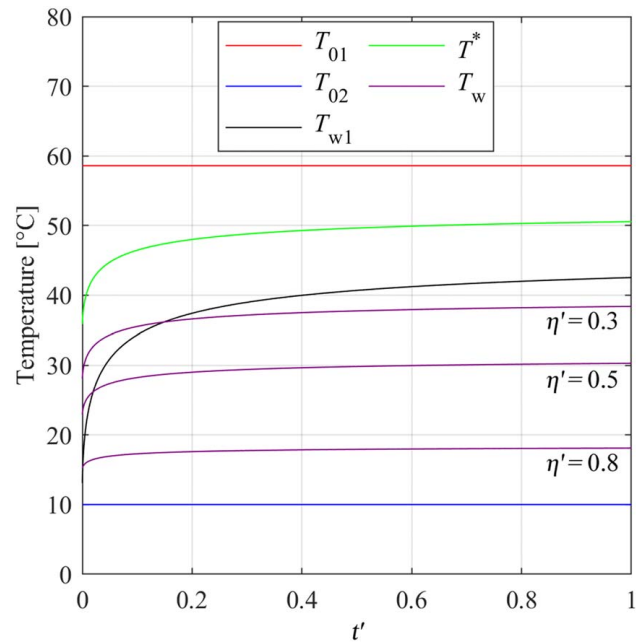


Fig. 16 Simulated temperature traces for the idealized virtual experiment (using $\eta^*_{TRUE} = 0.5$ and $T_{01}/T_{02} = 1.20$) used as the base case for the Monte Carlo analysis

calculated using Eq. (5), taking values of corrected film effectiveness equal to 0.3, 0.5, and 0.8. We refer to a particular true (input) value of corrected film effectiveness as η'_{TRUE} , and distinguish this from both the corresponding output value of the regression process (for a given pair of timestamps), η'_i , and the weighted average of the output values $\bar{\eta'}$. For completeness, we make a similar distinction between true (input) values of equivalent mainstream effectiveness, η^*_{TRUE} , and the corresponding weighted-average output values $\bar{\eta^*}$.

In this method, we use a particular constant value of η'_{TRUE} , and a definition of η' (Eq. (5)) that is applicable to an adiabatic surface. Thus, output wall temperatures respond instantly to the local driving gas temperature ($\tau = 0$). In systems with a nonadiabatic surface of interest, the surface temperature trace will lag behind (in time) the idealized adiabatic response with a time constant which depends on the material properties and local heat transfer coefficient. The delayed surface temperature response causes the calculated values of $\bar{\eta'}$ to be offset from the true value, by an amount that depends on the time constant of the delayed response. A further correction for this effect is therefore required if the surface

Table 2 Assumed values/ranges of temperatures and corresponding assumed absolute overall, bias, and precision uncertainties to 95% confidence for simulated virtual experiments

Parameter	Units	Value	U (K) 95%		
			Overall	Bias	Precision
T_{01}	K	340	± 0.5	$\pm \frac{0.5}{\sqrt{2}}$	$\pm \frac{0.5}{\sqrt{2}}$
T_{02}	K	283	± 0.5	$\pm \frac{0.5}{\sqrt{2}}$	$\pm \frac{0.5}{\sqrt{2}}$
T_{01}/T_{02}	—	1.2	—	—	—
T_w	K	283–340	± 1.0	$\pm \frac{1.0}{\sqrt{2}}$	$\pm \frac{1.0}{\sqrt{2}}$
T_{w1}	K	283–316	± 0.5	$\pm \frac{0.5}{\sqrt{2}}$	$\pm \frac{0.5}{\sqrt{2}}$

of interest is nonadiabatic. This is discussed in Appendix B. For the present analysis, we consider the case of a perfectly adiabatic surface. This condition can be approximately met in practice by using very low conductivity materials such as Rohacell.

The 1000 virtual experiments were created by superimposing bias and precision uncertainties on the idealized virtual experiment. To generalize the problem, and to highlight the importance of sampling at sufficiently high rates to drive down the precision uncertainty in the mean, we take values of *absolute overall uncertainty* as defined in Table 1, but ascribe equal contributions to bias and precision uncertainty. This would be representative of processing single data points from an experiment: that is, processing a single IR camera image, and taking a single sample of thermocouple measurements (no averaging of electronic noise). The resulting input uncertainty bands are given in Table 2, as are the test conditions for the idealized virtual experiment.

To create the virtual experiments, bias uncertainties (offset) were selected with appropriate weight from the normal distribution defined in Table 2, leading to an offset of the entire time history of the idealized virtual experiment. Precision uncertainty (noise) was added in a similar manner but with offsets applied to individual timestamps. This process was performed on every temperature measurement in the idealized virtual experiment, then repeated to create 1000 virtual experiments. The virtual experiments were then processed with varying timestamp number, as we will now describe.

Taking the 1000 virtual experiments as the base data set, the proposed methodology was applied to every virtual experiment for N in the range $2 < N < 50$. Timestamps at $t' = 1$ (end of the run) and $t' = 0.03$ (equivalent to 1 s after the mainstream temperature rise) were used for all runs, with timestamps being evenly distributed between these values for $N > 2$.

We now give an example of the analysis for the surface temperature trace corresponding to $\eta'_{\text{TRUE}} = 0.5$ in Fig. 16, for 1000 virtual experiments, and for the particular value $N = 50$. A histogram of the 1000 output weighted-average values $\bar{\eta}'$ is given in Fig. 17. The results are presented in equal buckets of η' (increments of $\eta' = 0.0016$) and show an approximately normal distribution centered on the input value $\eta'_{\text{TRUE}} = 0.5$, with standard deviation 0.0097, or overall uncertainty (to 95% confidence) of 0.0016.

Performing a similar process for $N = 2$ to $N = 50$, we determine values of absolute overall uncertainty (95% confidence) in $\bar{\eta}'$ as a

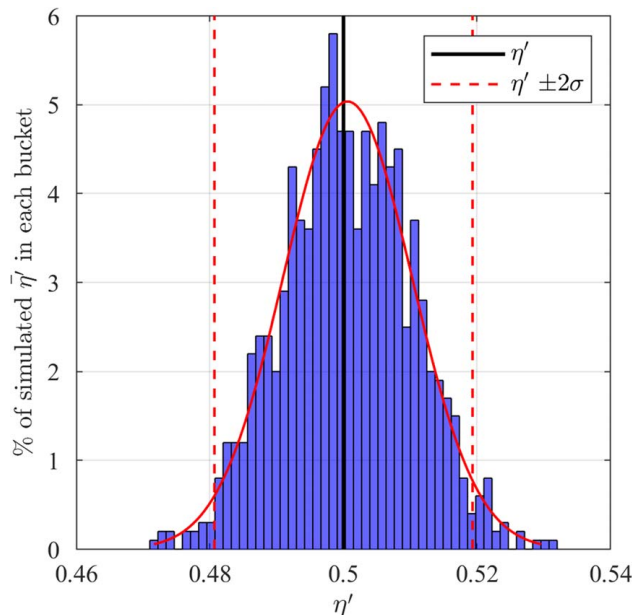


Fig. 17 Histogram of values of $\bar{\eta}'$ calculated for 1000 virtual experiments for $N = 50$, presented in equal buckets of η' (increments of $\eta' = 0.0016$)

function of N , for input values $\eta'_{\text{TRUE}} = 0.3, 0.5$, and 0.8 , and a sample of 1000 virtual experiments.

The uncertainty—for a particular value N —is determined by calculating the limits that include 95% of the samples in a particular distribution of the general form of Fig. 17 (example for $N = 50$). Results are plotted in Fig. 18 for $N = 2$ to $N = 50$. The general trend in overall uncertainty in $\bar{\eta}'$ is very similar (both qualitatively and quantitatively) for all three values of η'_{TRUE} , starting at a value of approximately 0.048, for $N = 2$, and decaying somewhat asymptotically to a value of 0.019, for $N = 50$. The impact of increasing the sampling number from $N = 2$ to $N = 50$ reduces the overall uncertainty in $\bar{\eta}'$ by approximately 3/5.

Ascribing all of the overall uncertainty to either bias or precision (instead of the equal weighting of Table 2) gives rise to the limiting trends shown in Fig. 18. This shows, at least for the particular sampling strategy chosen (in which optimal timestamps are used), that there is no benefit from increased sampling number if the bias uncertainty is the only contribution to overall uncertainty. This result may be considered surprising, but can be explained as follows. If a perfectly adiabatic surface is assumed, the surface temperature is instantaneously quasi-steady ($\tau = 0$) with respect to the fluid temperatures, and it can be shown that the resulting surface temperature response for particular η' and η^* is still a perfect solution for the system (albeit for values η' and η^* different from the input values), even when offset by a fixed temperature error (a bias error). A bias error (offset) in any measured temperature therefore results in the returned (output) value $\bar{\eta}'$ being offset from input (actual measured or simulated) η'_{TRUE} . The offset does not depend on the sampling strategy for the reasons given. In the example 1000 cases presented here, the absolute overall uncertainty, to 95% confidence, in $\bar{\eta}'$ when only bias errors are present is 0.0119.

If we relax the assumption that the surface is perfectly adiabatic, then T_w will have a time constant different to that of T^* leading to a lag of the surface temperature response with respect to the driving gas temperature response. In this case, a wall temperature with a bias error offset will no longer be a perfect solution for alternate pairings of η' and η^* and we would expect the absolute overall uncertainty to depend on the sampling strategy (particular timestamp pairs).

When precision uncertainty is the only contribution to overall uncertainty, increased timestamp number significantly reduces overall uncertainty. The trend is asymptotic, theoretically

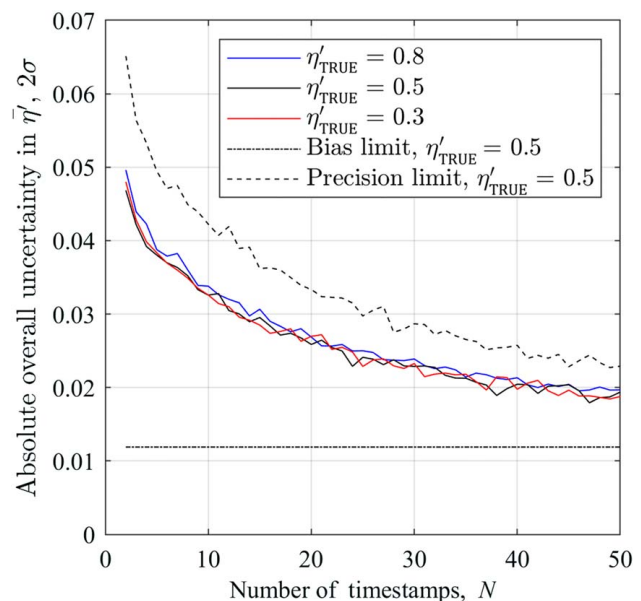


Fig. 18 Absolute overall (bias and precision) uncertainty in $\bar{\eta}'$ (95% confidence) for $\eta'_{\text{TRUE}} = 0.3, 0.5$, and 0.8 based on a population of 1000 virtual experiments, and $2 < N < 50$

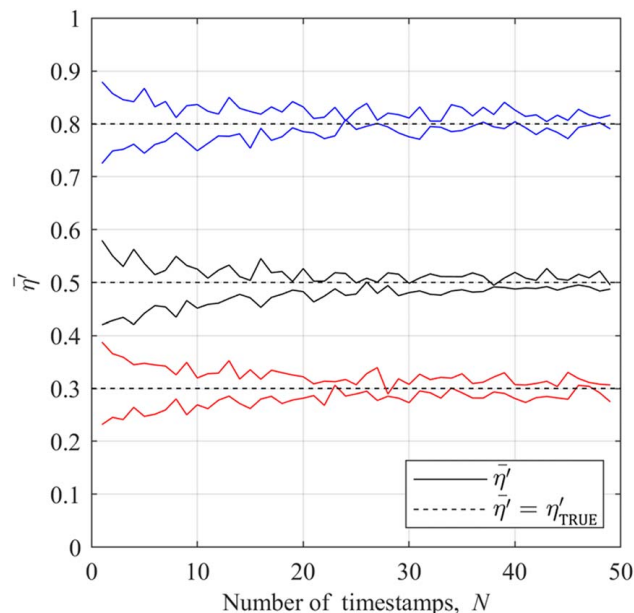


Fig. 19 Values of $\bar{\eta}'$ from 2 of 1000 virtual experiments for input values of $\eta'_{\text{TRUE}} = 0.3, 0.5$, and 0.8 and $2 < N < 50$

approaching 0 as $N \rightarrow \infty$, but limited in practice by the sampling frequency of individual variables, and by computational time for high N . For the idealized experiment presented here, and in the case when precision uncertainty is the only contribution to overall uncertainty, the absolute overall uncertainty reduces from 0.065 when $N=2$ to 0.023 when $N=50$. For $N=300$ (not shown), the absolute overall uncertainty is halved again (to approximately 0.011), but at an approximately 50-fold increase in computational cost. Even in experiments with high sampling rates, it is impossible to entirely eliminate precision error, and therefore reasonably high N would always be a sound choice. We now demonstrate this using simulated data realistic of an actual experiment.

To demonstrate the reduction in uncertainty in $\bar{\eta}'$ with increasing timestamp number, example results from two particular virtual experiments (input values in Table 2) are plotted in Fig. 19 for $\eta'_{\text{TRUE}} = 0.3, 0.5$, and 0.8 . The two particular virtual experiment examples were selected to have $\bar{\eta}'$ significantly different from the true value η'_{TRUE} for $N=2$. We see that as N increases, although there is some random-walk element in the decay of the trends (caused by precision uncertainty), the data collapse so that for $N=50$, $\bar{\eta}' \approx \eta'_{\text{TRUE}}$. Similar results would be expected in all real experiments.

Conclusions

In this paper, we present a new method to calculate adiabatic film effectiveness in the presence of an inlet thermal boundary layer. The general problem is that in systems with distorted inlet temperature (perhaps due to a cool thermal boundary layer) the convection and mixing processes are complex, and it is impossible to measure the hot gas temperature relevant to each point on the surface. In this situation, conventional processing methods (which use a single reference hot gas temperature) can overestimate or underestimate the true value of adiabatic film effectiveness. The arising error generally has both a temporal and a spatial element. This makes interpretation of the data problematic.

In the proposed method, the problem is overcome by calculating an *equivalent mainstream temperature*, T^* , for every point on the surface as a function of time. This is expressed using a new parameter which we refer to as *equivalent mainstream effectiveness*, η^* . This can be thought of as a nondimensional expression for T^* in

terms of the core gas temperature and the wall temperature. In our method, the equivalent mainstream effectiveness and the *corrected adiabatic film effectiveness* η' are solved simultaneously using data from two or more timestamps during the unsteady process of the wall accommodating to the local mixed temperature. The method works even in the case of time-varying inlet distortion, but is more accurate when the time constant of the thermal boundary layer is significantly greater than the time constant of the surface.

Using real experimental data from a high-pressure transonic blowdown linear cascade, we show that the proposed method produces adiabatic film effectiveness distributions which are more physically meaningful than conventional methods.

Using a numerical experiment that is a low-order simulation of a typical heat transfer experiment, we show that uncertainty in η' can be minimized by maximizing mainstream-to-coolant temperature ratio T_{01}/T_{02} ; selecting data timestamps which have significant temperature differences between upstream wall reference temperature measurements T_{w1} ; and selecting data timestamps in which the upstream wall reference temperature is significantly different to the coolant supply temperature. The first condition is limited by experimental facility capability. In general, the second and third conditions are achieved by selecting one early timestamp, between 0.23 and 1.20 time constants of the inlet thermal boundary layer, and one timestamp near the end of the heated period of the run. We show that in a well-conditioned experimental setup, the overall absolute uncertainty in η' can be below 0.022.

We demonstrate a further reduction in uncertainty in the proposed method by taking more than two timestamps and calculating a weighted average of results, based on their RSS uncertainties. Through analysis of 1000 virtual experiments with normal uncertainty distributions superimposed on idealized temperature traces, we show that the absolute overall uncertainty of the weighted average, $\bar{\eta}'$, can be significantly reduced when a large number of timestamps are used. For 50 timestamps, a reduction in uncertainty of 3/5 was achieved over the case with two timestamps.

There are many examples in the literature of adiabatic film effectiveness distributions measured in the presence of a significant inlet boundary layer. Conventional processing methods return measurements with potentially significant errors arising from this effect. The proposed method should significantly increase accuracy of the adiabatic film effectiveness returned in any experiment with significant distortion of the inlet temperature profile.

Acknowledgment

The authors gratefully acknowledge Rolls-Royce plc and Innovate UK for funding the research that led to this work.

Conflict of Interest

There are no conflicts of interest.

Data Availability Statement

The authors attest that all data for this study are included in the paper.

Appendix A: Extension to Compressible Flow

In compressible flows, there is a static temperature variation within the boundary layer caused by the so-called recovery effect: that is, in the frame of reference of the wall, there is bulk kinetic energy reduction and an associated increase in the mean molecular speed or static temperature. This static temperature variation through the boundary layer can be thought of as being superimposed on the existing thermal gradient, and changes the conductive and convective heat transfer within the boundary layer. We refer to the recovery temperature distribution, $T_{01,R}$, of the surface, which is

a function of Prandtl number of the fluid and the local Mach number

$$T_{01,R} = T_{01} \left[\frac{1 + r \left(\frac{\gamma - 1}{2} \right) M^2}{1 + \left(\frac{\gamma - 1}{2} \right) M^2} \right] \quad (\text{A1})$$

where r is the compressible recovery factor which is commonly taken as $r = \text{Pr}^{1/2}$ and $r = \text{Pr}^{1/3}$ for laminar and turbulent boundary layers, respectively [10]. The Mach number is a function of position and therefore the recovery temperature should properly be expressed as $T_{01,R}(x, t) = f(M(x), \text{Pr}(x))T_{01}(t)$, where x represents the surface position. For a particular environment with fixed Mach number distribution and defined boundary layer state, we can simplify this to $T_{01,R}(x, t) = f(x)T_{01}(t)$, i.e., the local recovery temperature is a function of surface position and the local mainstream total temperature.

In an environment with a mixing coolant film, in which the Mach number and Prandtl distributions have been determined *in the presence of the mixing film*, it would be natural to define the local total temperature *at the wall surface* in terms of the recovery temperatures of both the mainstream fluid and the cooling fluid, that is

$$T_{w,c}(x, t) = \eta_c(x)f(x)T_{02}(t) + (1 - \eta_c(x))f(x)T_{01}(t) \quad (\text{A2})$$

or, equivalently

$$T_{w,c}(x, t) = \eta_c(x)T_{02,R}(x, t) + (1 - \eta_c(x))T_{01,R}(x, t) \quad (\text{A3})$$

where η_c is the mass fraction of coolant in the near-wall fluid and $(1 - \eta_c)$ is the corresponding mass fraction of mainstream fluid. While η_c should strictly also be specified as a function of time—i.e., $\eta_c(x, t)$ —in the most general case, in an experiment in which the aerodynamic field is steady, we can simplify to $\eta_c(x)$ as in Eqs. (A2) and (A3). Here we also make the simplification of the same specific heat for both coolant and mainstream, but note that Eq. (A2) could easily be extended to the situation where there is a difference in the values of specific heats. Rearranging Eq. (A2), we can show that η_c can be interpreted as a *compressible adiabatic film effectiveness*

$$\eta_c(x) = \frac{f(x)T_{01}(t) - T_{w,c}(x, t)}{f(x)T_{01}(t) - f(x)T_{02}(t)} \quad (\text{A4})$$

or, restating Eq. (A4) directly in terms of the recovery temperatures, we have

$$\eta_c(x) = \frac{T_{01,R}(x, t) - T_{w,c}(x, t)}{T_{01,R}(x, t) - T_{02,R}(x, t)} \quad (\text{A5})$$

The form (A5) is discussed in a small number of papers (for example, Refs. [17,18]), but it is far more common to assume that the mixing coolant flow is *not* subject to recovery effects, and to use T_{02} in place of $T_{02,R}$ in Eq. (A5) (see, for example, Refs. [11,19]). Nonetheless, the form in Eq. (A4) preserves the link between the adiabatic film effectiveness and the mass fraction of coolant and mainstream fluids at a surface location—a physically tangible concept—and is therefore compatible with mass fraction based methods of the type used in this paper.

We now take this preferred *general* definition of compressible adiabatic film effectiveness and develop expressions for corrected compressible adiabatic film effectiveness necessary in the situation which is both compressible and has a time-varying inlet thermal boundary layer.

First, we define a *compressible equivalent mainstream temperature*, T_c^* , in analogy to Eq. (3), by

$$T_c^*(x, t) = \eta_c^*(x, t)T_{w1,R}(x, t) + (1 - \eta_c^*(x, t))T_{01,R}(x, t) \quad (\text{A6})$$

where $T_{w1,R}(x, t) = f(x)T_{w1}(t)$, i.e., the recovery temperature at a compressible location x , of a streamline originating from the location of the upstream wall reference temperature. Here, $T_c^*(x, t)$ is

the result at a particular surface location of the mixing of streamlines from within the thermal boundary layer. In Eq. (A6), η_c^* and $1 - \eta_c^*$ can be thought of as mass fractions of gas originating from locations instantaneous at the temperature of the upstream wall at the reference location, $T_{w1}(t)$, and at the core-flow temperature, $T_{01}(t)$, respectively. Rearranging for *compressible equivalent mainstream effectiveness* $\eta_c^*(x, t)$, we get

$$\eta_c^*(x, t) = \frac{T_{01,R}(x, t) - T_c^*(x, t)}{T_{01,R}(x, t) - T_{w1,R}(x, t)} \quad (\text{A7})$$

In analogy to Eq. (5), we can define a compressible corrected adiabatic film effectiveness

$$\eta'_c(x, t) = \frac{T_c^*(x, t) - T_{w,c}(x, t)}{T_c^*(x, t) - T_{02,R}(x, t)} \quad (\text{A8})$$

where parameters in the incompressible environment $T^*(x, t)$, $T_w(x, t)$, and $T_{02}(t)$ become equivalent parameters in the compressible environment $T_c^*(x, t)$, $T_{w,c}(x, t)$, and $T_{02,R}(x, t)$. For a steady aerodynamic flow field, η'_c and η_c^* can be assumed to be approximately constant in time allowing us to equate values at any two timestamps A and B, i.e.

$$\eta'_c(x) = \eta'_{c,A}(x) = \eta'_{c,B}(x) \quad (\text{A9})$$

$$\eta_c^*(x) = \eta_{c,A}^*(x) = \eta_{c,B}^*(x) \quad (\text{A10})$$

Using Eqs. (A4)–(A10) we can derive an expression for $\eta_c^*(x)$ —compressible parallel of Eq. (10)—in terms of measured temperatures and $f(x)$, where $f(x)$ is calculated from, for example, CFD or supplementary experiment (Mach number distribution required). We can then use Eq. (A6) to obtain $T_c^*(x, t)$, and Eq. (A8) to obtain $\eta'_c(x)$.

If the surface Mach number distribution is not known from CFD or a supplementary experiment (i.e., $f(x)$ not known) then provided additional timestamps are used (three or more), it is possible to extract $f(x)$ at the same time as $\eta_c^*(x)$ and $\eta'_c(x)$. That is, we solve for three variables simultaneously. This introduces additional sensitivities which would need to be assessed.

Appendix B: Correction for Nonadiabatic Surface Behavior

In this section, we quantify the error in the value of corrected adiabatic film effectiveness determined by our method in the case of nonadiabatic surface behavior. That is, the error in the result if nonadiabatic behavior is *not* accounted for. We refer to the extracted values in the case of nonadiabatic behavior as *inferred* (by the method) values.

Materials used in adiabatic film effectiveness studies are typically selected for their low values of thermal conductivity, k , and thermal inertia, $(\rho ck)^{1/2}$, which result in approximately adiabatic behavior. Nonetheless, no material is perfectly adiabatic, and this leads to heat transfer into the surface and a time-lag between the surface temperature response and the driving gas temperature response. The surface time constant is a function of k and $(\rho ck)^{1/2}$, and the local heat transfer coefficient, h . The surface time constant is lower at lower values of k and $(\rho ck)^{1/2}$ and at higher h . True adiabatic behavior, with $\tau = 0$, occurs for $(\rho ck)^{1/2} = 0$ or $h = \infty$.

The idealized virtual experiment, discussed above (see Fig. 16 and context), is replotted in Fig. 20 for an adiabatic surface, and for a surface with material properties of glass-filled nylon ($k = 0.28$, $(\rho ck)^{1/2} = 730 \text{ J/(m}^2 \text{ K s}^{1/2})$), with $h = 600$, 1200, and 1800 W/(m² K). For all cases, we specify input values $\eta_{\text{TRUE}} = 0.5$, $\eta_{\text{TRUE}}^* = 0.5$, and a time constant for T_{01} equal to zero. The driving gas temperature, which is the equivalent mainstream temperature (T^*), was calculated with the specified input values $T_{01}(t)$, $T_{02}(t)$, η_{TRUE} , and η_{TRUE}^* . This driving temperature is equal to the adiabatic surface response $T_w(t)$, shown by the dashed line in Fig. 20. The surface temperature responses for the

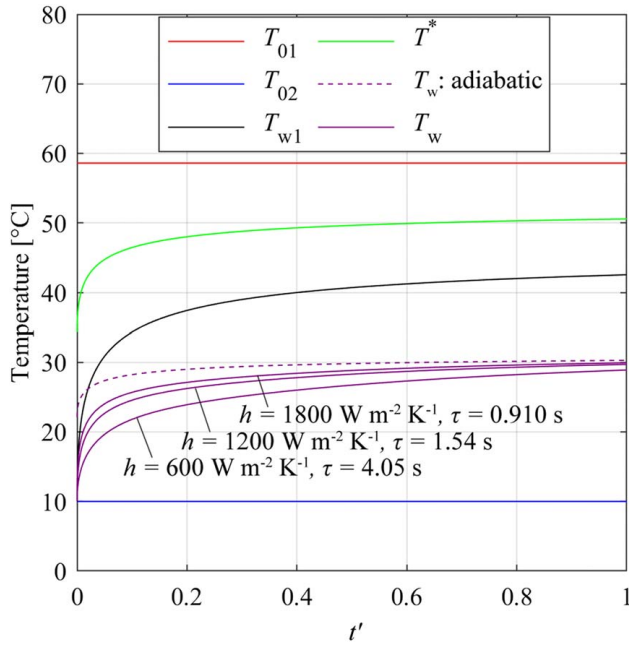


Fig. 20 Simulated surface temperature for adiabatic and non-adiabatic surfaces using thermal properties of glass-filled nylon: $(\rho ck)^{1/2} = 730 \text{ J/(m}^2 \text{ K s}^{1/2})$. Simulation conditions: $\eta'_{\text{TRUE}} = 0.5$; $\eta^*_{\text{TRUE}} = 0.5$; and $T_{01}/T_{02} = 1.20$.

nonadiabatic surface were calculated using a one-dimensional semi-infinite transient conduction model implemented in MATLAB (purple lines). As expected, there is a time-lag with respect to the driving temperature which increases as h decreases.

The method of this paper assumes an adiabatic surface response. Processing the simulated nonadiabatic surface responses of Fig. 20 using this same method, and failing to account for the nonadiabatic behavior, results in *inferred* output values (from virtual experiment) $\bar{\eta}'_{\text{INFERRED}}$ which are different from the true (input to virtual experiment) values, η'_{TRUE} . In the same way, inferred output values of $\bar{\eta}^*_{\text{INFERRED}}$ are different from the true (input) values of η^*_{TRUE} .

For target surface materials with large values of k and $(\rho ck)^{1/2}$, or very low h , the time constant of the target surface can exceed that of T_{w1} and best-fit solutions to the equations become nonphysical. In this situation, solutions with $\bar{\eta}^*_{\text{INFERRED}} > 1$ are possible, for example, representing an apparent driving temperature, T^*_{INFERRED} , lower than the upstream wall reference temperature. These nonphysical solutions can be stable, in that using different timestamps, or a greater number of timestamps, will still result in the same (incorrect) inferred pair $\bar{\eta}^*_{\text{INFERRED}}$ and $\bar{\eta}'_{\text{INFERRED}}$ for a given surface temperature response.

We define the *offset error* as the difference between the output from the proposed method and input values of corrected adiabatic effectiveness, i.e., $\bar{\eta}'_{\text{INFERRED}} - \eta'_{\text{TRUE}}$. This offset error can be estimated by using a series of virtual experiments. As an example, we do this for every value of η'_{TRUE} for four commonly used surface materials (Macor; GF nylon; acrylic; and Rohacell) of differing k and $(\rho ck)^{1/2}$, but for fixed values $\eta^*_{\text{TRUE}} = 0.5$, and $h_{\text{TRUE}} = 1200 \text{ W/(m}^2 \text{ K)}$. In our method we choose 50 timestamps, evenly distributed between optimal first and last timestamps. Results are shown in Fig. 21.

The offset values are everywhere negative, with larger offsets for larger values of $(\rho ck)^{1/2}$ (larger nonadiabatic tendency) and for smaller η'_{TRUE} . We also note that inferred values of equivalent mainstream effectiveness, $\bar{\eta}^*_{\text{INFERRED}}$, are greater than η^*_{TRUE} (not shown) and hence the inferred equivalent mainstream temperature, T^*_{INFERRED} , is lower than the true value at any given timestamp. The offset error reduces in magnitude as η'_{TRUE} increases, because when the wall temperature is closer to the coolant temperature errors in the driving hot gas temperature have reduced effect. For larger values of

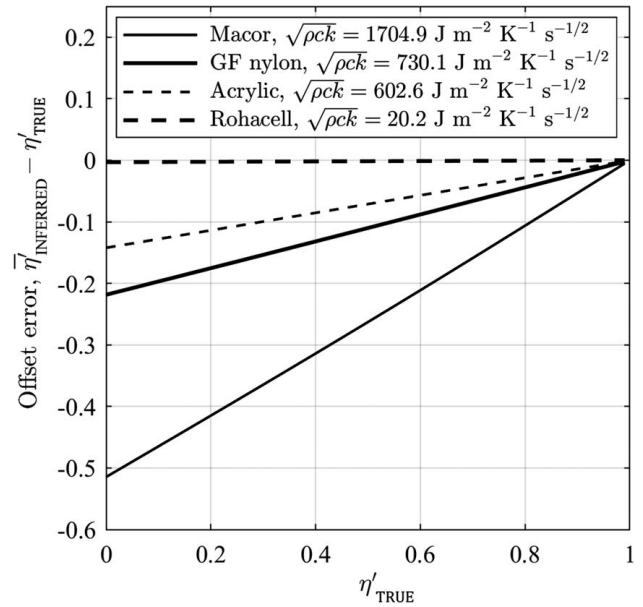


Fig. 21 Offset error $\bar{\eta}'_{\text{INFERRED}} - \eta'_{\text{TRUE}}$ plotted as a function of η'_{TRUE} for four materials commonly used in adiabatic film effectiveness experiments, for $\eta^*_{\text{TRUE}} = 0.5$, and $h_{\text{TRUE}} = 1200 \text{ W/(m}^2 \text{ K)}$

$(\rho ck)^{1/2}$, the surface time constant is greater, for a given value of h , resulting in greater errors in T^*_{INFERRED} . Although materials like Rohacell, are almost perfectly adiabatic (offset values less than 0.003 for all η'_{TRUE}), we see that for Acrylic the maximum offset is approximately 0.14, and worsens considerably for glass-filled Nylon and Macor. Without further correction (below), many common materials would give unacceptable error in this method.

For an experiment with known material properties and distribution of external surface heat transfer coefficient, by modeling the surface response, we can perform a first-order correction to the inferred values $\bar{\eta}'_{\text{INFERRED}}$, to remove the principal component of the offset error ($\bar{\eta}'_{\text{INFERRED}} - \eta'_{\text{TRUE}}$). We now attempt such a correction and refer to the resulting *best estimate* of adiabatic film effectiveness as

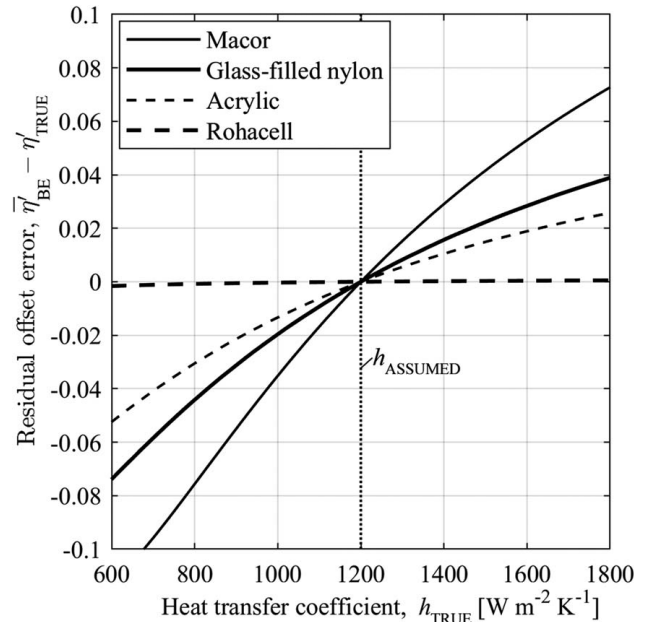


Fig. 22 Residual offset error ($\bar{\eta}'_{\text{BE}} - \eta'_{\text{TRUE}}$) for four materials for $\eta^*_{\text{TRUE}} = 0.5$, $\eta^*_{\text{TRUE}} = 0.5$, $h_{\text{ASSUMED}} = 1200 \text{ W/(m}^2 \text{ K)}$ plotted over the range $600 < h_{\text{TRUE}} < 1800 \text{ W/(m}^2 \text{ K)}$

$\bar{\eta}'_{BE}$. For semi-infinite surfaces, in the absence of lateral conduction, and for known h , the correction could be performed without error ($\bar{\eta}'_{BE} = \eta'_{TRUE}$). We characterize the error in the best estimate result, $\bar{\eta}'_{BE} - \eta'_{TRUE}$, for semi-infinite surfaces, in the absence of lateral conduction, for surfaces where the actual value of h (h_{TRUE}) is different from the assumed value, $h_{ASSUMED}$ used to model the surface response. We call the quantity $\bar{\eta}'_{BE} - \eta'_{TRUE}$ the *residual offset error*. Results for four materials are plotted in Fig. 22 for input values $\eta'_{TRUE} = 0.5$, $\eta'^*_{TRUE} = 0.5$, and $h_{ASSUMED} = 1200 \text{ W/(m}^2 \text{ K)}$, for the range of values $600 < h_{TRUE} < 1800 \text{ W/(m}^2 \text{ K)}$.

At the condition $h_{TRUE} = h_{ASSUMED}$, the residual offset error is zero. That is, our best estimate value $\bar{\eta}'_{BE}$ is equal to the true value η'_{TRUE} . This is trivially the case because, in the situation in which the assumed and true values of h are the same, our characterization of the offset error $\bar{\eta}'_{INFERRED} - \eta'_{TRUE}$ is perfect. The residual offset error increases both as $|h_{TRUE} - h_{ASSUMED}|$ increases (departure of true surface response from assumed surface response) and as $(\rho ck)^{1/2}$ and k increase. We see that for values h_{TRUE} within 10% of the assumed value, the maximum residual offset errors are 0.020, 0.011, 0.008, and 0.000 for the four materials discussed. In contrast, the corresponding absolute offset errors (Fig. 21) are 0.263, 0.110, 0.071, and 0.002. That is, by using a surface response model to estimate the correction term, the absolute errors can be reduced to approximately 1/10th of their original value.

Nomenclature

c	= specific heat capacity, J/(kg K)
h	= heat transfer coefficient, W/(m ² K)
k	= thermal conductivity, W/(m K)
r	= compressible recovery factor, dimensionless
t	= time, s
x	= surface location, m
M	= Mach number, dimensionless
N	= number of timestamps used in regression, dimensionless
T	= static temperature, K
U	= absolute overall uncertainty, various
\mathcal{R}	= recovery and redistribution parameter, dimensionless
$h_{ASSUMED}$	= assumed heat transfer coefficient for modeling surface response, W/(m ² K)
t_1	= start time of heated period, s
t_2	= end time of heated period, s
T_0	= total temperature, K
T_{01}	= core-flow temperature, taken as a proxy for the mainstream temperature, K
T_{02}	= coolant supply total temperature, K
$T_{01,R}$	= recovery temperature of core-flow, K
$T_{02,R}$	= recovery temperature of coolant flow, K
T_{w1}	= upstream wall reference temperature, K
T_w	= surface temperature at point of interest, K
$T_{w,ad}$	= adiabatic surface temperature, K
$T_{w,c}$	= surface temperature at point of interest in compressible flow environment, K
$T_{w1,R}$	= recovery temperature of upstream wall reference, K
$T_{\mathcal{R}}$	= recovery and redistribution temperature, K
t'	= nondimensional time, referred to heated period, dimensionless
T^*	= equivalent mainstream temperature, K
T^*_c	= equivalent mainstream temperature in compressible flow environment, K
Pr	= Prandtl number, dimensionless

Greek Symbols

γ	= isentropic exponent of gas, dimensionless
η	= adiabatic film effectiveness, dimensionless

η'	= corrected adiabatic film effectiveness, dimensionless
η'_c	= corrected adiabatic film effectiveness in compressible flow environment, dimensionless
$\bar{\eta}'$	= weighted-average corrected adiabatic film effectiveness from multiple timestamp method, dimensionless
η^*	= equivalent mainstream effectiveness, dimensionless
η^*_c	= equivalent mainstream effectiveness in compressible flow environment, dimensionless
$\bar{\eta}^*$	= weighted-average equivalent mainstream effectiveness from multiple timestamp method, dimensionless
$\bar{\eta}'_{BE}$	= "best estimate" equivalent mainstream effectiveness after correction for nonadiabatic behavior, dimensionless
ρ	= density, kg/m ³
σ	= standard deviation, various
τ	= time constant, s

Subscripts

A	= evaluated at timestamp A
ASSUMED	= value assumed for modeling surface response (esp. in nonadiabatic situation)
B	= evaluated at timestamp B
c	= referred to compressible flow conditions
INFERRED	= values obtained through application of proposed methods (esp. in nonadiabatic situation)
R	= referred to compressible recovery condition
TRUE	= values specified as inputs to model or assumed to be true from supplementary experiment

Abbreviations

PS	= pressure surface of rotor blade
RSS	= root-sum-squared
SS	= suction surface of rotor blade

References

- [1] Ornano, F., and Povey, T., 2020, "Theory of Non-Dimensional Groups in Film Effectiveness Studies," *ASME J. Turbomach.*, **142**(4), p. 041002.
- [2] Parker, J. A., Romero, E., and Povey, T., 2019, "A Modular Transonic Turbine Cascade for Cooled Rotor Metal Effectiveness Investigations," ASME Paper No. GT2019-91697.
- [3] Baldauf, S., Schulz, A., and Wittig, S., 1999, "High-Resolution Measurements of Local Effectiveness From Discrete Hole Film Cooling," *ASME J. Turbomach.*, **123**(4), pp. 758–765.
- [4] Ramesh, S., Ekkad, S., Straub, D. L., Lawson, S. A., and Alvin, M. A., 2014, "Experimental and Computational Analysis of Film Cooling Hole Performance on a High Temperature Test Rig," *Proceedings of the ASME 2014 International Mechanical Engineering Congress and Exposition*, Montreal, Quebec, Canada, Nov. 14–20, Volume 8B, p. V08BT10A007.
- [5] Facchini, B., Tarchi, L., Toni, L., and Ceccherini, A., 2010, "Adiabatic and Overall Effectiveness Measurements of an Effusion Cooling Array for Turbine Endwall Application," *ASME J. Turbomach.*, **132**(4), p. 041008.
- [6] Vedula, R. P., and Metzger, D. E., 1991, "A Method for the Simultaneous Determination of Local Effectiveness and Heat Transfer Distributions in Three Temperature Convective Situations," ASME Paper No. 91-GT-345.
- [7] Ekkad, S. V., Ou, S., and Rivir, R. B., 2004, "A Transient Infrared Thermography Method for Simultaneous Film Cooling Effectiveness and Heat Transfer Coefficient Measurements From a Single Test," *ASME J. Turbomach.*, **126**(4), pp. 597–603.
- [8] Holgate, N., Ireland, P., and Romero, E., 2019, "An Experimental-Numerical Method for Transient Infrared Measurement of Film Cooling Effectiveness and Heat Transfer Coefficient in a Single Test," *Aeronaut. J.*, **123**(1270), pp. 1982–1998.
- [9] Holgate, N., Ireland, P., and Romero, E., 2018, "The Effects of Combustor Cooling Features on Nozzle Guide Vane Film Cooling Experiments," *ASME J. Turbomach.*, **141**(1), p. 011005.
- [10] Kays, W., Crawford, M., and Weigand, B., 2004, *Convective Heat and Mass Transfer*, McGraw-Hill Higher Education, New York.
- [11] Xue, S., Roy, A., Ng, W. F., and Ekkad, S. V., 2015, "A Novel Transient Technique to Determine Recovery Temperature, Heat Transfer Coefficient, and Film Cooling Effectiveness Simultaneously in a Transonic Cascade," *ASME J. Therm. Sci. Eng. Appl.*, **7**(1), p. 011016.

- [12] Luque, S., Jones, T. V., and Povey, T., 2016, "Theory for the Scaling of Metal Temperatures in Cooled Compressible Flows," *Int. J. Heat Mass Transfer*, **102**(1), pp. 331–340.
- [13] Luque, S., Jones, T. V., and Povey, T., 2017, "Scaling of Turbine Metal Temperatures in Cooled Compressible Flows—Experimental Demonstration of a New Theory," *ASME J. Turbomach.*, **139**(8), p. 081001.
- [14] Michaud, M., Ornano, F., Chowdhury, N. H. K., and Povey, T., 2019, "Methodology for High-Accuracy Infrared Calibration in Environments With Through-Wall Heat Flux," *J. Global Power Propul. Soc.*, **4**(1), pp. 1–13.
- [15] Friedrichs, S., Hodson, H. P., and Dawes, W. N., 1997, "Aerodynamic Aspects of Endwall Film-Cooling," *ASME J. Turbomach.*, **119**(4), pp. 786–793.
- [16] Kirollos, B., and Povey, T., 2017, "Laboratory Infrared Thermal Assessment of Laser-Sintered High-Pressure Nozzle Guide Vanes to Derisk Engine Design Programs," *ASME J. Turbomach.*, **139**(4), p. 041009.
- [17] Goldstein, R. J., 1971, "Film Cooling: Adiabatic Wall Temperature and Film Cooling Effectiveness," *Adv. Heat Transfer*, **7**(1), pp. 326–330.
- [18] Dellimore, K. H., Marshall, A. W., and Cadou, C. P., 2010, "Influence of Compressibility on Film-Cooling Performance," *J. Thermophys. Heat Transfer*, **24**(3), pp. 506–515.
- [19] Furukawa, T., and Ligrani, P. M., 2002, "Transonic Film Cooling Effectiveness From Shaped Holes on a Simulated Turbine Airfoil," *J. Thermophys. Heat Transfer*, **16**(2), pp. 228–237.